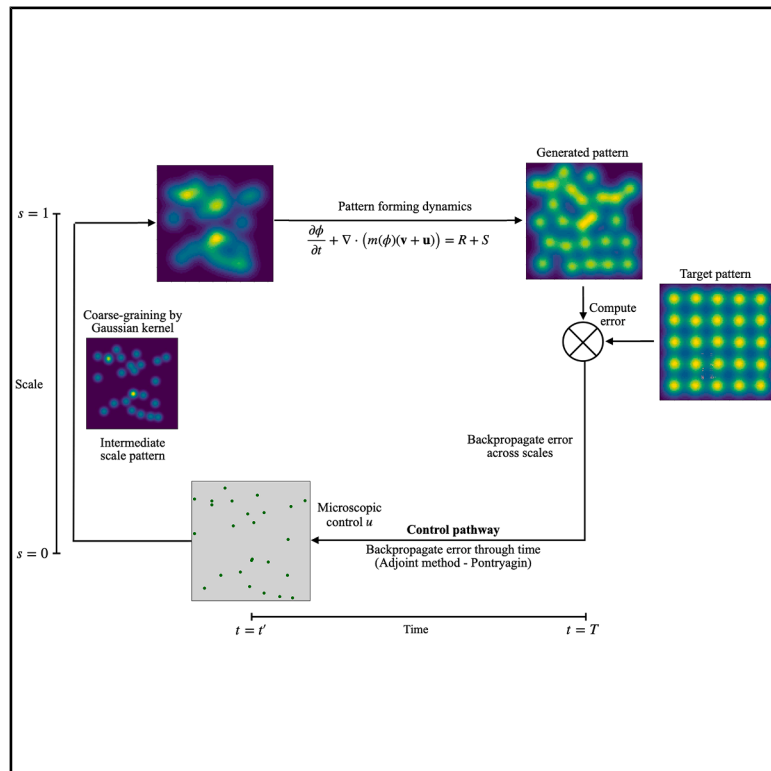


# Hamiltonian bridge for scale-dependent optimal control of particles and fields

## Graphical abstract



## Authors

Vishaal Krishnan, Sumit Sinha, L. Mahadevan

## Correspondence

lmahadev@g.harvard.edu

## In brief

Complex spatiotemporal patterns are a central theme in the physics of non-equilibrium systems. Krishnan et al. propose a physics-based framework that unifies particle and field descriptions for generative control of non-equilibrium patterns. Field-level objectives are actuated at the particle level, and the adjoint-based path integral control computes efficient gradients. The resulting Hamiltonian bridge produces energy- and conservation-aware interpolations between target and initial states demonstrated across phase separation, reaction-diffusion, droplet self-assembly, and tissue-like morphogenesis.

## Highlights

- Unified particle-field control via an Eulerian-Lagrangian loop
- Adjoint-based path integral control (APIC) scales stochastic control
- Hamiltonian bridge yields physics-respecting pattern interpolations
- Validated on phase separation, reaction-diffusion, and morphogenesis

Article

# Hamiltonian bridge for scale-dependent optimal control of particles and fields

Vishaal Krishnan,<sup>1,4</sup> Sumit Sinha,<sup>1,2,4</sup> and L. Mahadevan<sup>1,3,5,\*</sup>

<sup>1</sup>School of Engineering and Applied Sciences, Harvard University, Cambridge, MA 02138, USA

<sup>2</sup>Department of Data Science, Dana-Farber Cancer Institute, Boston, MA, USA

<sup>3</sup>Departments of Physics, and Organismic and Evolutionary Biology, Harvard University, Cambridge, MA 02138, USA

<sup>4</sup>These authors contributed equally

<sup>5</sup>Lead contact

\*Correspondence: [lmahadev@g.harvard.edu](mailto:lmahadev@g.harvard.edu)

<https://doi.org/10.1016/j.newton.2025.100365>

**ACCESSIBLE OVERVIEW** Patterns in non-equilibrium systems—from phase separation to tissue morphogenesis—arise from microscopic stochastic dynamics but are most easily specified and measured at macroscopic scales. This work introduces a unified physics-based framework for generative control of such patterns that bridges particle (Lagrangian) and field (Eulerian) descriptions. Starting from overdamped Langevin dynamics for interacting particles with internal states, this work defines smoothed mesoscopic fields and a free-energy functional that governs macroscopic evolution. The resulting flows are projected back to particles via smoothed-particle hydrodynamics, closing a micro-macro modeling loop. Control objectives are posed at the field level but actuated at the particle level, enabling scale-dependent design. To solve the resulting high-dimensional stochastic control problem, an adjoint-based path integral control (APIC) is introduced, which marries an exact Feynman-Kac linearization of the Hamilton-Jacobi-Bellman (HJB) equation with continuous-time backpropagation and automatic differentiation to compute exact gradients of the value functional from sampled trajectories. Instead of solving the full HJB equation, APIC samples uncontrolled trajectories forward and propagates adjoint co-states backward to compute control gradients efficiently. The controlled dynamics define a Hamiltonian bridge: a physically constrained interpolation between initial and target patterns that respects conservation laws and energetic structure. The framework is demonstrated across canonical systems—navigation on complex landscapes, Allen-Cahn (non-conserved) and Cahn-Hilliard (conserved) phase separation, thin-film droplet self-assembly, reaction-diffusion patterning, and a cell-fate/migration model—showing scalable control and interpretable transport geometries. Conceptually, this links generative modeling and optimal control with variational physics, offering a route to programmable pattern formation in soft matter, active media, and developmental systems and suggesting a path toward inference-in-the-loop and experimental actuation.

## SUMMARY

Many-body particle systems and pattern-forming fields far from equilibrium generate complex spatiotemporal structures whose function we may wish to evoke, optimize, or steer. We introduce a multiscale optimal control framework that unifies particle- and field-level descriptions via a tunable Eulerian-Lagrangian coarse graining. Starting from microscopic Langevin dynamics for particles with internal states, we construct smoothed-pattern fields and a field-level free energy, then project the resulting dynamics back to particles using smoothed-particle hydrodynamics. This micro-macro loop lets us pose control tasks at the field level while simulating and actuating them at the particle level in a physically consistent way. To solve the resulting high-dimensional stochastic control problems, we develop adjoint-based path integral control (APIC), which combines a Feynman-Kac formulation with continuous-time backpropagation and automatic differentiation to compute gradients of the value function via forward sampling and backward adjoint propagation. The controlled dynamics define a Hamiltonian bridge—a physically constrained interpolation between initial and target patterns—yielding a generative view of pattern control shaped by the energy landscape. We demonstrate our framework on controlled navigation on complex landscapes, conservative

## and non-conservative phase separation, droplet self-assembly, coupled reaction-diffusion systems, and a model of spatiotemporal tissue differentiation.

### INTRODUCTION

The spontaneous emergence of complex spatiotemporal patterns from simple local interactions is a central theme in the physics of non-equilibrium systems, with manifestations across physics, chemistry, biology, and engineering.<sup>1</sup> Over the past century, the study of pattern formation has revealed that general mathematical principles—such as symmetry breaking, conservation laws, and gradient flows—can transcend specific applications. Originally framed in the context of equilibrium phase transitions by Landau,<sup>2</sup> these ideas have since been extended to physical,<sup>3</sup> chemical,<sup>4</sup> material,<sup>5</sup> and biological systems.<sup>6</sup> A natural approach to this program starts with microscopic dynamics using Langevin or master equations and yields macroscopic evolution equations through coarse-graining and variational closures.<sup>7,8</sup> This theory-rich, data-poor framework has had enormous success in explaining spontaneous pattern formation in natural and engineered systems. In parallel, the last decade has seen the rise of data-rich, theory-poor generative models that can synthesize complex patterns by learning from large datasets.<sup>9</sup> These include methods based on optimal transport,<sup>10,11</sup> unbalanced transport,<sup>12</sup> normalizing flows,<sup>13–15</sup> and diffusion-based probabilistic models.<sup>16</sup> While powerful, these models typically do not incorporate physical constraints such as conservation laws and material constitutive relations, and are thus agnostic to the basic mechanisms of spontaneous symmetry breaking and are difficult to interpret. Recent work has begun to probe the internal structure of these models,<sup>17</sup> but the absence of physical priors limits their applicability to real-world physical systems. Complementing these advances in the physical sciences and engineering, the study of the emergence of collective functionality in living systems—ranging from morphogenesis to behavior—requires regulation and feedback<sup>18</sup> and raises the question of whether the ideas and notions of many-body statistical physics and continuum field theories can be deployed effectively to understand and eventually control biophysical processes. In particular, there is an increasing interest in changing perspectives from the forward problem of predicting pattern evolution to the inverse problem of controlling pattern formation.<sup>19–21</sup> Control must account for both microscale mechanisms and macroscale constraints, leading to a fundamentally multiscale problem: how to specify the microscopic interactions (e.g., among molecules or cells) that give rise to emergent patterns, given that control of function is often easiest to specify at large scales but needs to be implemented on small scales. This raises the question: how can we build physically grounded generative models for pattern control over a range of scales spanning the dynamics of interacting particles to macroscopic spatiotemporal fields?

Here, we present a coarse-grained optimal control framework that connects microscopic and macroscopic dynamics via a Eulerian-Lagrangian modeling loop. Starting from the coupled Langevin dynamics for particle positions and internal states, we define emergent pattern fields through kernel-based smoothing to formulate a field-level free energy that governs macro-

scopic dynamics. We then project the resulting flows, which allow for a variational interpretation, back to the microscopic level using smoothed particle hydrodynamics (SPH). This modeling loop enables us to formulate control objectives at the field level—where patterns and functionality reside—while enacting them through fine-scale particle dynamics in a physically consistent way.

To solve the resulting high-dimensional stochastic control problem, we introduce an adjoint-based path integral control (APIC) algorithm. APIC combines the classical Feynman-Kac formulation of stochastic optimal control<sup>22–25</sup> with continuous-time backpropagation<sup>26–28</sup> and automatic differentiation frameworks such as JAX.<sup>29,30</sup> Unlike standard path integral or sampling-based control methods,<sup>31,32</sup> which rely on Monte Carlo estimators without gradient information, APIC computes exact gradients of the value functional by backward-propagating adjoint co-states along sampled trajectories. This allows for efficient gradient-based evaluation of control inputs even in systems with many interacting degrees of freedom, mitigating the curse of dimensionality that limits classical dynamic programming approaches. As a result, APIC enables scalable and physically grounded control of complex stochastic systems evolving on high-dimensional energy landscapes. Our primary contribution is to synthesize and unify a number of different existing approaches, e.g., statistical and continuum dynamics of particles and fields, control theory (Pontryagin principle and Hamilton-Jacobi-Bellman [HJB] equations), and advanced numerical algorithms (autodifferentiation and tensor computations) for solving forward-backward equations via sampling, to provide an interpretable framework for programming materials.

Our approach connects to a broad class of systems where control problems take the form of guided navigation through complex energy landscapes. These include the control of classical and quantum spins,<sup>33–35</sup> protein folding and allostery,<sup>36–38</sup> directed evolution,<sup>39</sup> soft robotics,<sup>40</sup> metamaterial design,<sup>41–44</sup> swarm control,<sup>45,46</sup> and learning in neural networks.<sup>47</sup> All these can be characterized as many-body systems evolving in high-dimensional, stochastic, and structured landscapes. We apply our framework to a range of pattern-forming systems from soft and active matter, including navigation of interacting particles on a complex landscape, phase separation with conserved and non-conserved order parameters, droplet self-assembly via thin-film hydrodynamics, reaction-diffusion systems, and spatiotemporal tissue morphogenesis. Across these domains, our framework—which we call the Hamiltonian bridge—provides a generative, physically grounded method for pattern control that is capable of interpolation between initial and target states while respecting physical laws.

### RESULTS

#### Formulation of the optimal control problem

Many complex spatiotemporal patterns are fundamentally governed by microscopic stochastic dynamics describing the

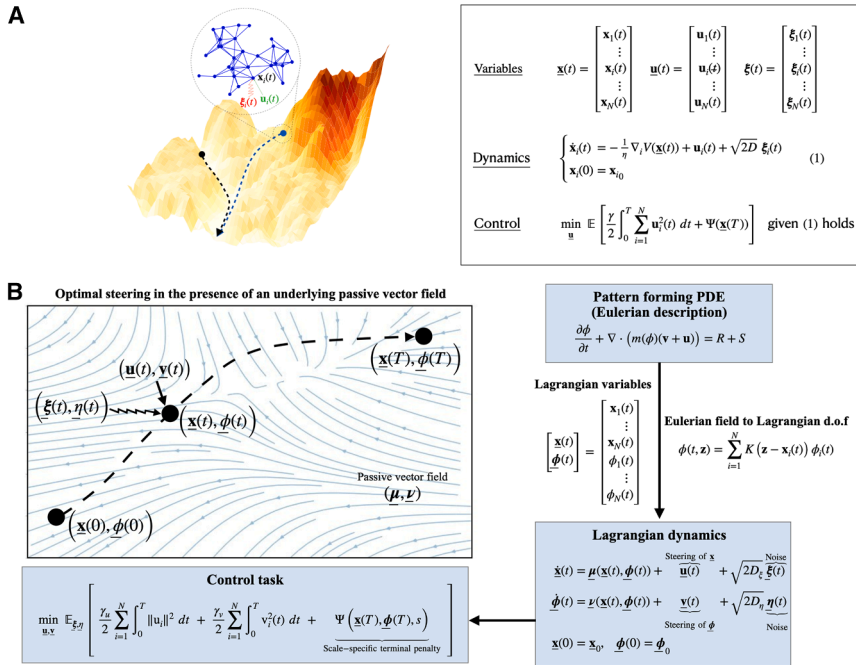


**Figure 1. Conceptual framework for coarse-grained control**

(A) Navigation of an interacting particle system (blue network of nodes and edges) on a complex landscape (see Note S2). In this schematic, the rugged terrain depicts the complex energy landscape, which the system is navigating. The blue network is a representation of the interacting particle system, where the blue nodes are particles (position depicted by  $\mathbf{x}_i(t)$ ) and the edges denote the interaction between the particles. The control  $\mathbf{u}_i(t)$  drives the system on the rugged landscape, which gives rise to distinct non-equilibrium phases. The noise of the environment is modeled by a delta-correlated white noise,  $\xi_i(t)$ . The system undergoes overdamped Langevin dynamics under the influence of potential,  $V(\mathbf{x}_1, \mathbf{x}_2, \dots, \mathbf{x}_N)$ , delta-correlated white noise ( $\xi_1, \xi_2, \dots, \xi_N$ ), and control ( $\mathbf{u}_1, \mathbf{u}_2, \dots, \mathbf{u}_N$ ). The control task is then to minimize the expectation ( $\mathbb{E}$ ) of a running cost  $\int_0^T \sum_{i=1}^N \|\mathbf{u}_i(t)\|^2 dt$  and a terminal cost  $\Psi(\mathbf{x}_1(T), \mathbf{x}_2(T), \dots, \mathbf{x}_N(T))$ , where the expectation is with respect to controlled trajectories. In the current study, we also formulate the optimal navigation for athermal,  $D = 0$ , many-body interacting systems. In this limit, the stochastic optimal control reduces to the deterministic case.

(B) Physics-driven framework for pattern generation

Top-right panel shows the general form of conserved and non-conserved PDEs considered in the present study. Here,  $\phi$  can be a scalar or vector valued field,  $\mathbf{v}$  is a known vector field modeling the intrinsic pattern-forming capacity,  $\mathbf{u}$  is the control flux field,  $R$  is a given reaction field, and  $S$  is the control reaction field as described in Rezende and Mohamed.<sup>16</sup> The pattern control objective is formulated as the steering of the pattern generated by the forward dynamics toward a target pattern as described in Song et al.<sup>16</sup> In the Eulerian-Lagrangian control formulation, the Eulerian field  $\phi(t, \mathbf{z})$  is first discretized via the smoothed particle hydrodynamics (SPH) method (see Note S4) to Lagrangian degrees of freedom (dofs),  $\mathbf{x}_i$  and  $\phi_i$ , which when deployed on the Eulerian PDE lead to a set of coupled non-linear equations for the Lagrangian dofs (see Note S4). The Lagrangian dofs are then steered via  $\mathbf{u}$  and  $\mathbf{v}$  to obtain the target field via the optimal control objective. The Eulerian-Lagrangian optimal control formulation can be viewed as navigation on a complex landscape as shown on the left.

evolution of both positional and internal degrees of freedom, and the macroscopic patterns they generate are best understood and controlled at the level of a coarse-grained field. Our approach begins with a coupled stochastic description of particle positions and internal states, which we refer to as the microscopic dynamics. We then apply a local kernel-based coarse-graining procedure to define an emergent field variable that captures mesoscopic pattern structure. This field evolves via a gradient flow with respect to an effective free-energy functional, whose form is motivated by statistical averaging of the underlying particle interactions. To simulate and control the system efficiently, we project the coarse-grained free energy back onto the microscopic degrees of freedom using the same smoothing kernel, yielding particle-level equations that faithfully encode macroscopic pattern dynamics. This modeling loop—linking microscale dynamics to macroscale energetics and back—provides a physically grounded and computationally tractable foundation for optimal control of pattern formation across scales.

We begin with the Lagrangian description of a system given by  $N$  interacting particles moving in a spatial domain  $\Omega \subset \mathbb{R}^d$ , where each particle carries both a positional degree of freedom  $\mathbf{x}_i(t) \in \Omega$  and an internal state  $\phi_i(t) \in \mathbb{R}$ . The microscopic configuration is given by  $\mathbf{x}(t) = (\mathbf{x}_1(t), \dots, \mathbf{x}_N(t))$  and  $\phi(t) = (\phi_1(t), \dots, \phi_N(t))$  (see Figure 1 for a schematic). In the absence of control, we assume that the system evolves according to the overdamped Langevin equations:

$$\begin{aligned} \dot{\mathbf{x}}(t) &= -\nabla_{\mathbf{x}} V(\mathbf{x}(t), \phi(t)) + \sqrt{2D_{\xi}} \xi(t), \\ \dot{\phi}(t) &= -\nabla_{\phi} V(\mathbf{x}(t), \phi(t)) + \sqrt{2D_{\eta}} \eta(t), \end{aligned} \quad (\text{Equation 1})$$

where  $V(\mathbf{x}, \phi)$  is a microscopic interaction potential encoding both positional and internal couplings, and  $\xi(t)$  is a vector of zero-mean Gaussian white noise processes. These equations model stochastic relaxation on the energy landscape  $V$ , with thermal noise controlled by the diffusion coefficient  $D_{\xi}$ . In this setting, the system samples from the Gibbs-Boltzmann equilibrium distribution  $P(\mathbf{x}, \phi) \propto \exp(-V/D_{\xi})$ , and pattern formation arises from the interplay of interactions, noise, and dissipation.

To create a coarse-grained Eulerian description, we define a mesoscopic scalar field  $\phi(t, \mathbf{z})$  by locally averaging the internal states of particles using a smoothing kernel:

$$\phi(t, \mathbf{z}) := \sum_{i=1}^N \phi_i(t) \kappa(\mathbf{z} - \mathbf{x}_i(t)), \quad (\text{Equation 2})$$

where  $\kappa(\cdot)$  is a non-negative kernel (e.g., Gaussian or spline) centered at the origin and normalized such that  $\int \kappa(\mathbf{z}) d\mathbf{z} = 1$ . The kernel bandwidth  $\sigma(s)$  determines the smoothing scale, with  $s \in [0, 1]$  interpolating between fine- and coarse-grained

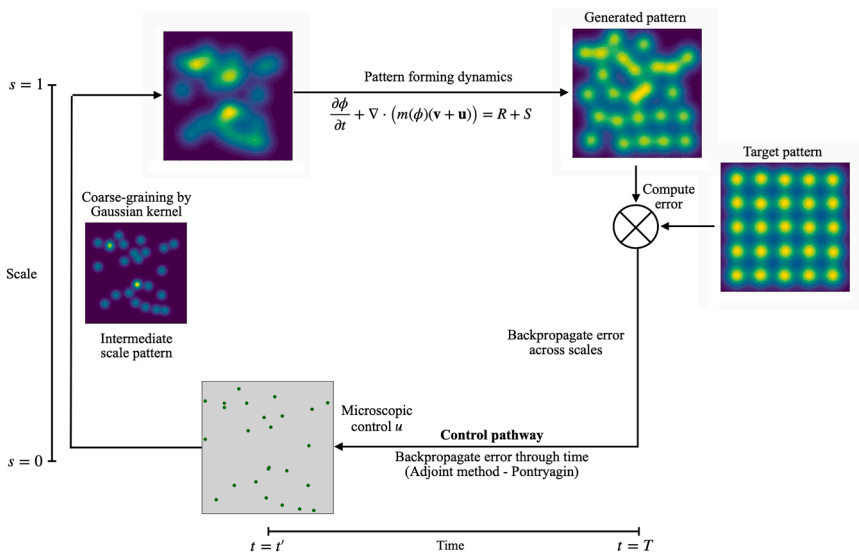


**Figure 2. Physics-driven framework for pattern generation**

Mathematical formulation of Eulerian-Lagrangian control formulation. The Eulerian field  $\phi(t, \mathbf{z})$  is discretized via SPH method to Lagrangian degrees of freedom (dofs),  $\mathbf{x}_i$  and  $\phi_i$ . Utilizing the Eulerian PDE, we obtain the coupled non-linear dynamical system for Lagrangian dofs. The Lagrangian dofs are then steered via  $\mathbf{u}$  and  $\mathbf{v}$  to obtain the target field via the optimal control objective. The Eulerian-Lagrangian optimal control formulation can be viewed as navigation on a complex landscape.

resolutions (see Figure 2 for the schematic). The field  $\varphi$  may represent, for instance, a density, concentration, or cell-fate fraction, depending on the application.

In the Eulerian description, we now seek a variational description of the macroscopic pattern dynamics in terms of a free-energy functional  $E[\varphi]$  that captures the effective energetics of the coarse-grained field. This free energy inherits contributions from the microscopic interaction potential as well as entropic effects due to Brownian motion. The corresponding free energy has the form

$$E[\varphi] = \int_{\Omega} \left[ (D_{\varepsilon} + D_{\eta}) \varphi(\mathbf{z}) \log \varphi(\mathbf{z}) + U(\varphi(\mathbf{z})) + \frac{\varepsilon}{2} \|\nabla \varphi(\mathbf{z})\|^2 \right] d\mathbf{z}, \quad (\text{Equation 3})$$

where the first term arises from configurational entropy,  $U(\varphi)$  is an effective potential derived from the interaction energy (e.g., a double-well potential for phase separation), and the gradient term penalizes spatial inhomogeneities, capturing interfacial energy from short-range interactions. The passive dynamics of the field  $\varphi$  then follow a gradient flow on  $E$  denoted by  $\frac{\partial \phi}{\partial t} = - \frac{\delta E}{\delta \varphi} \Big|_{\varphi = \phi}$ . We

note that  $\phi(t, \mathbf{z})$  denotes a state (pattern) trajectory of the system, whereas  $\varphi(\mathbf{z})$  is any arbitrary point in the space of allowable patterns (see Note S1 for notational clarity).

To complete the Eulerian-Lagrangian modeling loop, we now reverse the coarse graining and reconstruct a particle-level potential  $V(\mathbf{x}, \underline{\phi})$  that is consistent with the macroscopic free energy. This is done by substituting the kernel representation (Equation 2) into Equation 3, dropping the entropy term (which arises from integrating out microscopic fluctuations) and expressing the resulting energy as a function of  $(\mathbf{x}, \underline{\phi})$ :

$$V(\mathbf{x}, \underline{\phi}) := \int_{\Omega} \left[ U \left( \sum_{i=1}^N \phi_i \kappa(\mathbf{z} - \mathbf{x}_i) \right) + \frac{\varepsilon}{2} \left\| \nabla \sum_{i=1}^N \phi_i \kappa(\mathbf{z} - \mathbf{x}_i) \right\|^2 \right] d\mathbf{z}. \quad (\text{Equation 4})$$

This energy defines the particle-particle interactions such that the smoothed field  $\varphi(\mathbf{z})$  minimizes the original free energy  $E[\varphi]$ . In this way, we obtain a consistent variational principle across scales.

We now introduce control terms to steer the system from an initial state toward a desired target pattern. Let  $\mathbf{u}(t) \in \mathbb{R}^{Nd}$  be a control force acting on the particle positions and  $\mathbf{s}(t) \in \mathbb{R}^N$  a control field acting on the internal states. The controlled dynamics become

$$\begin{aligned} \dot{\mathbf{x}}(t) &= -\nabla_{\mathbf{x}} V(\mathbf{x}(t), \underline{\phi}(t)) + \mathbf{u}(t) + \sqrt{2D_{\varepsilon}} \xi(t), \\ \dot{\underline{\phi}}(t) &= -\nabla_{\underline{\phi}} V(\mathbf{x}(t), \underline{\phi}(t)) + \mathbf{s}(t) + \sqrt{2D_{\eta}} \eta(t), \end{aligned} \quad (\text{Equation 5})$$

with  $V(\mathbf{x}, \underline{\phi})$  as in Equation 4. These control terms modulate the particle trajectories and internal dynamics in order to shape the macroscopic field  $\varphi(t, \mathbf{z})$  over time. We formulate an optimal control problem that seeks to minimize a cost functional combining control effort and terminal accuracy (see Note S2). Let the desired target pattern be  $\varphi^*(\mathbf{z})$ . Using the kernel representation, the terminal cost becomes

$$\Psi(\mathbf{x}(T), \underline{\phi}(T)) := \int_{\Omega} \left\| \sum_{i=1}^N \phi_i(T) \kappa(\mathbf{z} - \mathbf{x}_i(T)) - \varphi^*(\mathbf{z}) \right\|^2 d\mathbf{z}, \quad (\text{Equation 6})$$

and the total cost functional is

$$\min_{\mathbf{u}, \mathbf{s}} \mathbb{E}_{\mathbf{Q}_{\mathbf{u}, \mathbf{s}}} \left[ \int_0^T \left( \frac{\gamma_u}{2} \|\mathbf{u}(t)\|^2 + \frac{\gamma_v}{2} \|\mathbf{s}(t)\|^2 \right) dt + \Psi(\mathbf{x}(T), \underline{\phi}(T)) \right], \quad (\text{Equation 7})$$

subject to the controlled dynamics (Equation 5). The weights  $\gamma_u, \gamma_v$  balance the cost of control with the terminal accuracy. This completes the Eulerian-Lagrangian modeling loop: (1) starting from microscopic Langevin dynamics, (2) we coarse-grain to define a mesoscopic field, (3) derive a variational law governing pattern evolution, (4) reconstruct a consistent microscopic potential, and (5) formulate an optimal control problem defined at the particle level but targeting macroscopic functionality. In the following section, we present a scalable algorithm for solving this high-dimensional stochastic control problem using APIC.

### APIC algorithm

We now describe our numerical strategy for solving the stochastic optimal control problem introduced above. Following the

positional and internal degrees of freedom. The product of  $D$  and  $\gamma$  defines the relative scale between intrinsic fluctuations and control effort. By equating the two, we assume that the controller is equally penalized relative to the noise in both sub-systems—a reasonable assumption in many soft-matter and biological contexts where spatial movement and internal transitions occur over comparable energy scales. Under this condition, the linearized backward PDE for  $W(t, \mathbf{x}, \underline{\phi})$  becomes

$$\frac{\partial W}{\partial t} + D_\xi \Delta_{\mathbf{x}} W + D_\eta \Delta_{\underline{\phi}} W - \nabla_{\mathbf{x}} V \cdot \nabla_{\mathbf{x}} W - \nabla_{\underline{\phi}} V \cdot \nabla_{\underline{\phi}} W = 0, \quad (\text{Equation 8})$$

with terminal condition  $W(T, \mathbf{x}, \underline{\phi}) = e^{-\beta \Psi(\mathbf{x}, \underline{\phi})}$ , where  $\Psi$  encodes the desired final configuration via projection from the target pattern field  $\varphi^*(\mathbf{z})$ . The solution admits a path integral representation via the Feynman-Kac formula<sup>23</sup> (see Notes S2 and S3)

$$W(t, \mathbf{x}, \underline{\phi}) = \mathbb{E}_{\mathbb{P}} \left[ e^{-\beta \Psi(\mathbf{x}(T), \underline{\phi}(T))} \left| \begin{array}{l} \dot{\mathbf{x}}(t') = -\nabla_{\mathbf{x}} V(\mathbf{x}(t'), \underline{\phi}(t')) + \sqrt{2D_\xi} \xi(t'), \\ \dot{\underline{\phi}}(t') = -\nabla_{\underline{\phi}} V(\mathbf{x}(t'), \underline{\phi}(t')) + \sqrt{2D_\eta} \eta(t'), \\ \text{with initial condition } (\mathbf{x}(t), \underline{\phi}(t)) = (\mathbf{z}, \phi) \end{array} \right. \right], \quad (\text{Equation 9})$$

standard approach in stochastic optimal control, the associated value function  $F(t, \mathbf{x}, \underline{\phi})$  satisfies an HJB equation (see Note S3) of the form

$$\frac{\partial F}{\partial t} + D \Delta F - \nabla F \cdot \nabla V - \frac{1}{2\gamma} |\nabla F|^2 = 0$$

along with the temporal boundary condition  $F(T, \mathbf{z}) = \Psi(\mathbf{z})$  which must therefore be solved in backward time from  $t = T$ . The HJB equation suffers from the curse of dimensionality owing to the nonlinearity and the state space being of dimension  $N \gg 1$ . To get around this, we apply the Cole-Hopf transformation,

$$F(t, \mathbf{x}, \underline{\phi}) = -\frac{1}{\beta} \log W(t, \mathbf{x}, \underline{\phi}),$$

which converts the non-linear HJB equation into a linear partial differential equation (PDE) (see Note S3) provided the inverse temperature  $\beta$  satisfies

$$\beta = \frac{1}{2\gamma_u D_\xi} = \frac{1}{2\gamma_v D_\eta}.$$

This condition ensures that the quadratic gradient terms arising from the cost functional precisely cancel, thereby linearizing the HJB equation in both  $\mathbf{x}$  and  $\underline{\phi}$ . Physically, this assumption corresponds to matching the effective temperature of the

where  $\mathbb{E}_{\mathbb{P}}$  is the expectation operator with respect to the distribution of uncontrolled paths. From the definition  $F = -\frac{1}{\beta} \log W$ , the optimal control laws are given by the gradients of the value function (see Note S2 for details)

$$\mathbf{u}^*(t) = -\frac{1}{\gamma_u} \nabla_{\mathbf{x}} F(t, \mathbf{x}(t), \underline{\phi}(t)), \mathbf{s}^*(t) = -\frac{1}{\gamma_v} \nabla_{\underline{\phi}} F(t, \mathbf{x}(t), \underline{\phi}(t)).$$

To compute these gradients efficiently, we propagate multiple trajectories of the uncontrolled dynamics from current state  $(\mathbf{x}(t), \underline{\phi}(t))$  forward in time, compute the gradients of  $\Psi$  at the terminal state, and backpropagate sensitivity information using an adjoint method. Specifically, we define scaled adjoint variables

$$\lambda_{\mathbf{x}}(t') = -\frac{1}{\beta W(t, \mathbf{x}, \underline{\phi})} \frac{\delta W}{\delta \mathbf{x}(t')}, \lambda_{\underline{\phi}}(t') = -\frac{1}{\beta W(t, \mathbf{x}, \underline{\phi})} \frac{\delta W}{\delta \underline{\phi}(t')},$$

and evolve them backward via

$$\begin{aligned} \dot{\lambda}_{\mathbf{x}}(t') &= \nabla_{\mathbf{x}} \nabla_{\mathbf{x}} V(\mathbf{x}(t'), \underline{\phi}(t')) \lambda_{\mathbf{x}}(t'), \\ \dot{\lambda}_{\underline{\phi}}(t') &= \nabla_{\underline{\phi}} \nabla_{\underline{\phi}} V(\mathbf{x}(t'), \underline{\phi}(t')) \lambda_{\underline{\phi}}(t'), \end{aligned} \quad (\text{Equation 10})$$

with terminal conditions

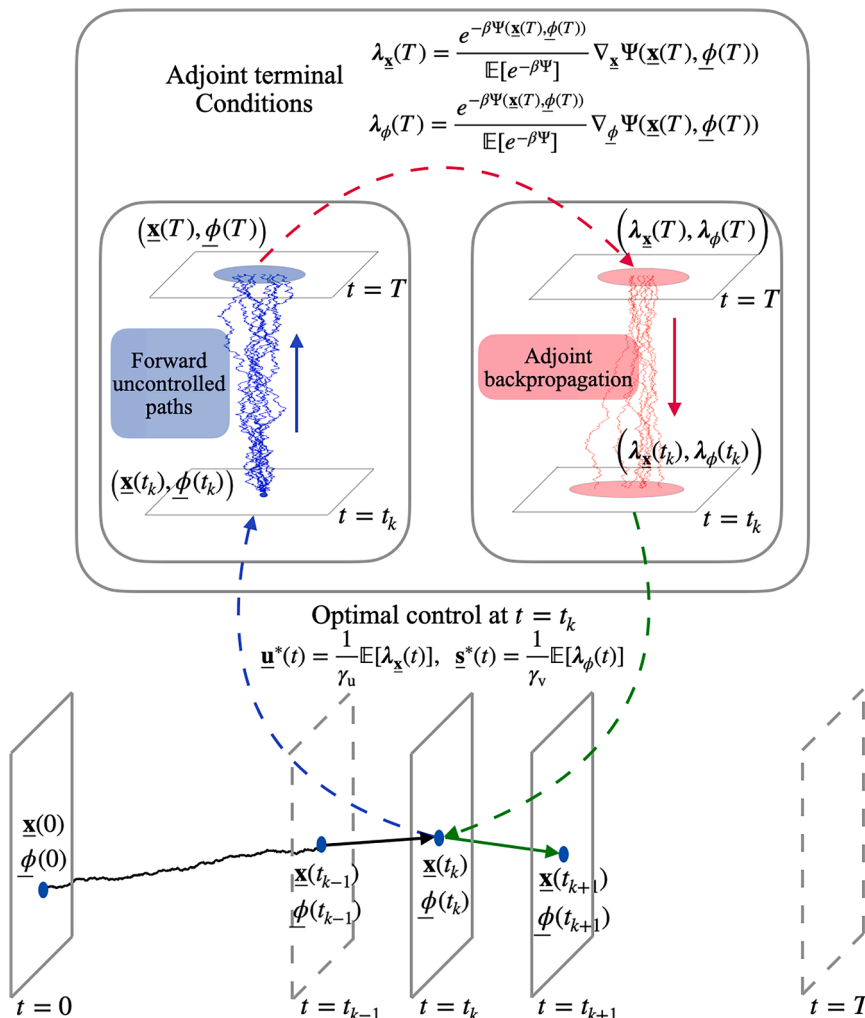


**Figure 3. Adjoint-based path integral control**

(Left) Schematic illustration of the adjoint path integral control (APIC) algorithm over a finite time horizon. At time  $t_0$ , several forward trajectories are sampled from the uncontrolled stochastic dynamics (Equation 1) using independent Brownian noise realizations. Each sampled trajectory evolves from the current state  $(\underline{x}(t_0), \underline{\phi}(t_0))$  to a terminal state at time  $T$ . At the final time, the terminal gradient of the cost function  $\Psi$  is evaluated and Boltzmann-weighted to initialize adjoint co-states. These co-states are then integrated backward in time along each path using the adjoint ODE (Equation 10). The optimal control inputs  $\underline{u}^*(t_0)$  and  $\underline{s}^*(t_0)$  are obtained as sample averages over the corresponding adjoint variables. This algorithm enables scalable stochastic control for high-dimensional many-body systems with both positional and internal degrees of freedom. Derivatives of the interaction potential  $V(\underline{x}, \underline{\phi})$  are computed via automatic differentiation using the JAX framework.<sup>29</sup> Trajectory sampling and ODE/SDE integration are performed using Diffrax,<sup>49</sup> with parallelization and vectorization handled through JAX's `vmap`.

$$\lambda_{\underline{x}}(T) = \frac{e^{-\beta\Psi(\underline{x}(T), \underline{\phi}(T))}}{\mathbb{E}[e^{-\beta\Psi}]} \nabla_{\underline{x}} \Psi(\underline{x}(T), \underline{\phi}(T)),$$

$$\lambda_{\underline{\phi}}(T) = \frac{e^{-\beta\Psi(\underline{x}(T), \underline{\phi}(T))}}{\mathbb{E}[e^{-\beta\Psi}]} \nabla_{\underline{\phi}} \Psi(\underline{x}(T), \underline{\phi}(T)).$$

(Equation 11)

Here,  $\nabla_{(\cdot)} \nabla_{(\cdot)}$  is the Hessian. Finally, the optimal controls at time  $t$  are computed by averaging these adjoint variables across samples

$$\underline{u}^*(t) = \frac{1}{\gamma_u} \mathbb{E}[\lambda_{\underline{x}}(t)], \quad \underline{s}^*(t) = \frac{1}{\gamma_v} \mathbb{E}[\lambda_{\underline{\phi}}(t)].$$

(Equation 12)

**Algorithm 1. Adjoint-based path integral control algorithm**

**Input:** Current time  $t$ , state  $(\underline{x}(t), \underline{\phi}(t))$ , number of sample paths  $n$   
**For each time  $t$ :**

- 1: Sample  $n$  independent noise trajectories  $(\underline{\xi}(t'), \underline{\eta}(t'))$  over  $t' \in [t, T]$
- 2: Simulate  $n$  forward trajectories using the uncontrolled dynamics (Equation 1)
- 3: For each terminal state, compute gradients of the terminal cost  $\Psi$  and set adjoint terminal conditions as in Equation 11
- 4: Integrate adjoint equations backward in time as in Equation 10
- 5: Compute optimal controls by averaging adjoint variables across samples, as in Equation 12

This completes the APIC algorithm for multiscale pattern-forming systems, now extended to internal degrees of freedom (see Figure 3 for the schematic). The key insight is that forward sampling of uncontrolled dynamics, combined with backward propagation of sensitivities, allows us to compute optimal control without solving the full HJB equation, thereby circumventing the curse of dimensionality.<sup>48</sup>

### Geometric and physical interpretation of the Hamiltonian bridge

#### Control of particles: Traversal along ridges

We now use a variational argument to suggest the emergence of a universal strategy. For simplicity, we consider the athermal limit of the stochastic optimal control problem (Equation 7) involving only the positional degrees of freedom, which then reduces to

$$\min_{\mathbf{u}} \frac{\gamma}{2} \int_0^T \|\mathbf{u}\|^2(t) dt + \Psi(\mathbf{x}(T)), \text{ s.t.}$$

$$\dot{\mathbf{x}}(t) = -\nabla V(\mathbf{x}(t)) + \mathbf{u}(t); \quad \mathbf{x}(0) = \mathbf{x}_0$$

(Equation 13)

Substituting  $\mathbf{u}(t) = \dot{\mathbf{x}}(t) + \nabla V(\mathbf{x}(t))$  into the functional (Equation 13) yields the following unconstrained minimization problem for  $\mathbf{x}$ :

$$\begin{aligned} \mathcal{L} &= \min_{\mathbf{x}} \frac{\gamma}{2} \int_0^T \|\dot{\mathbf{x}}(t) + \nabla V(\mathbf{x}(t))\|^2 dt + \Psi(\mathbf{x}(T)) \\ &= \min_{\mathbf{x}} \frac{\gamma}{2} \int_0^T \|\dot{\mathbf{x}}(t)\|^2 dt + \gamma \int_0^T \nabla V(\mathbf{x}(t))^T \cdot \dot{\mathbf{x}}(t) dt \\ &\quad + \frac{\gamma}{2} \int_0^T \|\nabla V(\mathbf{x}(t))\|^2 dt + \Psi(\mathbf{x}(T)). \end{aligned}$$

Setting  $\delta\mathcal{L}/\delta\mathbf{x} = 0$  yields following equation of motion for the optimal trajectory of the state  $\mathbf{x}(t)$ , given by

$$\ddot{\mathbf{x}}(t) = \nabla \nabla V(\mathbf{x}(t)) \nabla V(\mathbf{x}(t)) = \frac{1}{2} \nabla (\|\nabla V(\mathbf{x}(t))\|^2),$$

(Equation 14)

with  $\mathbf{x}(0) = \mathbf{x}_0$  and the terminal boundary condition  $\dot{\mathbf{x}}(T) = -\nabla V(\mathbf{x}(T)) - \frac{1}{\gamma} \nabla \Psi(\mathbf{x}(T))$ . Note that  $\nabla \nabla V = \partial_i \partial_j V$  denotes the Hessian of  $V$ . We note that Equation 14 is derived in the athermal limit (i.e., in the regime where the interaction scale is large compared to fluctuations). The emergent equation in the limit where fluctuations and interactions play an important role in tandem is an interesting question, which will be the focus of our subsequent studies.

The physical interpretation of the emergent (Equation 14) is that in flat regions of the landscape, the particle follows the simple geodesic straight-line path ( $\ddot{\mathbf{x}} = 0$ ), whereas in non-flat regions it accelerates in the direction of increasing magnitude of the gradient of  $V$ . Furthermore, the behavior is symmetric under the transformation  $V \rightarrow -V$  of the potential, which implies that hills and valleys of the landscape have the same effect.

#### Control of spatiotemporal fields: Transport along geodesics

Having formulated the optimal control problem at the microscopic level and constructed a consistent Eulerian-Lagrangian modeling loop, we now consider the projection of this framework to the macroscopic (field) level. In this setting, the coarse-grained pattern field  $\phi(t, \mathbf{z})$  evolves under physics-informed dynamics that may include both conserved and non-conserved processes. These dynamics capture a wide variety of pattern-forming systems, including phase separation, reaction-diffusion systems, and active matter. We consider the general form of the coarse-grained dynamics

$$\begin{aligned} \frac{\partial \phi}{\partial t}(t, \mathbf{z}) + \nabla \cdot \left( m(\phi) \left( \mathbf{v}(t, \mathbf{z}) + \underbrace{\mathbf{u}(t, \mathbf{z})}_{\text{conserved control flux}} \right) \right) \\ = R(t, \mathbf{z}) + \underbrace{S(t, \mathbf{z})}_{\text{non-conserved control source}}, \end{aligned}$$

(Equation 15)

where  $m(\phi)$  is a mobility,  $\mathbf{v}(t, \mathbf{z})$  is a passive flux (e.g., from chemical potential gradients), and  $R(t, \mathbf{z})$  is a non-conserved reaction field. The control inputs consist of a divergence-free control flux  $\mathbf{u}(t, \mathbf{z})$ , acting on conserved quantities, and a local reaction control  $S(t, \mathbf{z})$ , allowing non-conserved manipulations. In the uncontrolled case ( $\mathbf{u} = 0, S = 0$ ), this equation reduces to classical models such as Allen-Cahn, Cahn-Hilliard, or thin-film equations, depending on the specific choices of  $m(\phi)$  and  $R$ . These are often studied in terms of their ability to explain spontaneous pattern formation in a range of different physical, chemical, and biological systems.<sup>50</sup> However, in many of these settings—e.g., morphogenesis, synthetic biology, or materials programming—the goal is to actively design and control patterns. This motivates our formulation of a coarse-grained optimal control problem.

Given an initial field  $\phi_0(\mathbf{z})$  and a target pattern  $\phi^*(\mathbf{z})$ , we define a quadratic control cost functional that penalizes the control effort over the time horizon  $[0, T]$ :

$$C_{\gamma_u, \gamma_v}(t, \phi, \mathbf{u}, S) = \frac{\gamma_u}{2} \int_{\Omega} m(\phi) \|\mathbf{u}(t, \mathbf{z})\|^2 d^2 \mathbf{z} + \frac{\gamma_v}{2} \int_{\Omega} S(t, \mathbf{z})^2 d^2 \mathbf{z},$$

where  $\gamma_u$  and  $\gamma_v$  are weights controlling the trade-off between the two types of control effort. This cost structure reflects the physical distinction between transport-based and source-based actuation mechanisms. The macroscopic optimal control problem is then

$$\min_{\mathbf{u}, S} \int_0^T C_{\gamma_u, \gamma_v}(t, \phi, \mathbf{u}, S) dt, \text{ s.t. } \begin{cases} \frac{\partial \phi}{\partial t} + \nabla \cdot (m(\phi)(\mathbf{v} + \mathbf{u})) = R + S, \\ \phi(0, \mathbf{z}) = \phi_0(\mathbf{z}), \phi(T, \mathbf{z}) = \phi^*(\mathbf{z}). \end{cases} \quad (\text{Equation 16})$$

This formulation represents an infinite-dimensional optimal control problem for a PDE-constrained system, where the goal is to find minimal-cost control protocols that interpolate between prescribed patterns. Although the underlying field dynamics are not Hamiltonian in the classical sense, the structure of the

optimality conditions admits a Hamiltonian representation via Pontryagin's principle. Specifically, the optimal control strategy is characterized by the following coupled Hamiltonian system:

$$\frac{\partial \phi}{\partial t} = \frac{\delta H}{\delta \Lambda}, \quad \frac{\partial \Lambda}{\partial t} = -\frac{\delta H}{\delta \phi}, \quad (\text{Equation 17})$$

where  $\Lambda(t, \mathbf{z})$  is the co-state (adjoint field). We note that this is consistent with the Poisson bracket formulation of Hamiltonian systems.<sup>51</sup> The control Hamiltonian  $H(\varphi, \lambda)$  takes the form

$$H(\varphi, \lambda) = \int_{\Omega} \left[ m(\varphi) \nabla \lambda \cdot \mathbf{v} + \lambda R - \frac{m(\varphi)}{2\gamma_u} \|\nabla \lambda\|^2 - \frac{\lambda^2}{2\gamma_v} \right] d^2 \mathbf{z}. \quad (\text{Equation 18})$$

Here,  $\delta H / \delta \lambda$  and  $\delta H / \delta \varphi$  denote variational derivatives of the Hamiltonian with respect to the adjoint and state fields, respectively. These variational derivatives define the evolution of the system state and adjoint via the generalized Hamilton equations. This formalism can be viewed as an infinite-dimensional analog of the finite-dimensional canonical equations  $\dot{q} = \partial H / \partial p$ ,  $\dot{p} = -\partial H / \partial q$  but defined over function spaces. Furthermore, we distinguish here between two notational uses:  $(\phi(t), \Lambda(t))$  refers to a time-evolving state-co-state trajectory over  $[0, T]$ , whereas  $(\varphi, \lambda)$  refers to generic field and adjoint pairs when defining functionals. This macroscopic Hamiltonian formulation allows us to recast the terminal boundary value problem as a variational optimization over initial adjoint fields:

$$\begin{aligned} & \max_{\mathbf{x}_0} \int_{\Omega} \Lambda_0(\mathbf{z}) \phi_0(\mathbf{z}) \, d^2 \mathbf{z} - \int_{\Omega} \Lambda_T(\mathbf{z}) \phi^*(\mathbf{z}) \, d^2 \mathbf{z}, \\ \text{s.t.} \quad & \frac{\partial \phi}{\partial t} = \frac{\delta H}{\delta \Lambda}, \quad \frac{\partial \Lambda}{\partial t} = -\frac{\delta H}{\delta \phi}. \end{aligned} \quad (\text{Equation 19})$$

We refer to the optimal path  $\phi(t, \mathbf{z})$  that solves this system as the Hamiltonian bridge between the initial and final patterns. It provides a physically interpretable interpolation trajectory that respects the geometry of the control landscape and the thermodynamic constraints of the system. This coarse-grained variational structure complements the microscopic control framework described earlier and provides geometric insight into pattern transport in field space.

(A) Reaction field determines the nature of the interpolant for control of non-conserved order parameter dynamics. In the absence of any intrinsic pattern-forming capability in a system with a non-conserved order parameter,  $R = 0$ ,  $\mathbf{v} = 0$ , so that the target pattern can be fully steered via a non-conserved dynamics associated with a control reaction field  $S$ . The optimal control reaction field is then given by  $S = -\frac{1}{\gamma_v} \Lambda$ , where  $\frac{\partial \Lambda}{\partial t}(t, \mathbf{z}) = 0$ , i.e.,  $\Lambda(t, \mathbf{z}) = \Lambda_0(\mathbf{z})$  (see [Note S3.1](#) for details). From the terminal constraints in [Equation 16](#), we have  $\phi(0, \mathbf{z}) = \phi_0(\mathbf{z})$  and  $\phi(T, \mathbf{z}) = \phi^*(\mathbf{z})$ , so that  $\Lambda(t, \mathbf{z}) = \Lambda_0(\mathbf{z}) = \phi^*(\mathbf{z}) - \phi_0(\mathbf{z})$ , resulting in the optimal pattern evolution corresponding to a linear interpolation (for the case of nominal Hamiltonian  $H_0(\varphi, \lambda) = -\int_{\Omega} \frac{\lambda^2}{2\gamma_v} d^2 \mathbf{z}$ ) between  $\phi_0$  and  $\phi^*$ , i.e.,  $\phi(t, \mathbf{z}) = \phi_0(t, \mathbf{z}) + \frac{t}{T}(\phi^*(t, \mathbf{z}) - \phi_0(t, \mathbf{z}))$  for  $t \in [0, T]$ .

When the passive pattern-forming capacity is present, i.e., the reaction field  $R \neq 0$ , we obtain a modified path (with  $H_1(\varphi, \lambda) = \int_{\Omega} \lambda R d^2 \mathbf{z}$ ) for the controlled evolution of the pattern (see [Note S3.1](#) for details):

$$\begin{aligned} \phi(t, \mathbf{z}) &= \phi_0(t, \mathbf{z}) + \frac{t}{T}(\phi^*(t, \mathbf{z}) - \phi_0(t, \mathbf{z})) \\ &+ \int_0^t R(\tau, \mathbf{z}) d\tau - \frac{t}{T} \int_0^T R(\tau, \mathbf{z}) d\tau. \end{aligned} \quad (\text{Equation 20})$$

We can visualize this non-linear interpolation between  $\phi_0$  and  $\phi^*$  in the upper-right panel of [Figure 5](#) where the state trajectories corresponding to  $R = 0$  and  $R \neq 0$ , i.e., Allen-Cahn, are plotted, and note that our interpolant weights the passive physics and active control to achieve the final state with a minimum control cost.

(B) Effective potential determines path of pattern evolution in the case of conserved order parameter dynamics. In the absence of any intrinsic pattern-forming capability in a system with a conserved order parameter, i.e.,  $R = 0$ ,  $\mathbf{v} = 0$ , and  $\int_{\Omega} \phi_0 d^2 \mathbf{z} = \int_{\Omega} \phi^* d^2 \mathbf{z}$ , the target pattern can be fully steered via a conserved dynamics associated with a control flux  $\mathbf{u}$ . In the context of the Hamiltonian bridge formalism, we can interpret this in terms of a nominal Hamiltonian  $H_0$  and mobility  $m(\varphi) = \varphi$  (which corresponds to the dynamics for the conserved order-parameter case for any control vector field  $\mathbf{u}$ ), while the pattern-forming capacity via passive physics corresponds to an energetic contribution to the Hamiltonian  $H_1$ , with  $H = H_0 + H_1$ .

To investigate how this changes the geometry of pattern evolution, we note that the nominal control Hamiltonian (in the absence of pattern-forming capacity) for a conserved order-parameter pattern evolution is given by  $H_0(\varphi, \lambda) = -\frac{1}{2\gamma_u} \int_{\Omega} \varphi \|\nabla \lambda\|^2 d^2 \mathbf{z}$ . The adjoint/co-state equation then follows from [Equation 17](#) as  $\frac{\partial \Lambda}{\partial t} = -\frac{\delta H_0}{\delta \varphi}(\varphi, \Lambda)$  and simplifies to  $\frac{\partial \Lambda}{\partial t} - \frac{1}{2\gamma_u} \|\nabla \Lambda\|^2 = 0$ . This last equation for the co-state is identical to the equation for the fluid potential in the well-known Benamou-Brenier formulation of optimal transport<sup>8</sup> that uses a hydrodynamic framework to transform normalized probability distributions via flows. Taking the gradient of the equation yields a quasilinear equation for the gradient of the co-state  $\frac{\partial \nabla \Lambda}{\partial t} - \frac{1}{\gamma_u} \nabla \Lambda \nabla \Lambda = 0$  (note that  $\nabla \nabla \Lambda$  denotes the Hessian of  $\Lambda$ , and the term  $\nabla \nabla \Lambda \nabla \Lambda = (\partial_i \partial_j \Lambda) \partial_j \Lambda$  can be seen as the gradient of  $\frac{1}{2} \|\nabla \Lambda\|^2$ ), with characteristics given by the equation

$$\frac{d}{dt} \mathbf{x}^{\text{nom}}(t) = -\frac{1}{\gamma_u} \nabla \Lambda_0^{\text{nom}}(\mathbf{x}_0^{\text{nom}}), \quad \mathbf{x}^{\text{nom}}(0) = \mathbf{x}_0^{\text{nom}}, \quad (\text{Equation 21})$$

along which  $\frac{\partial}{\partial t} \nabla \Lambda(t, \mathbf{x}(t)) = 0$ , so that  $\nabla \Lambda(t, \mathbf{x}(t)) = \nabla \Lambda(0, \mathbf{x}_0) = \nabla \Lambda_0(\mathbf{x}_0)$ . Solving the characteristic equation allows us to infer that optimal pattern evolution occurs along straight lines (geodesics) given by  $\mathbf{x}(t) = \mathbf{x}_0 - \frac{t}{\gamma_u} \nabla \Lambda_0(\mathbf{x}_0)$ , where  $\Lambda_0$  can be computed from the terminal constraints  $\phi_0$  and  $\phi^*$  (see [Note S3.2](#) for details of the derivation).

In the presence of an intrinsic pattern-forming capacity associated with the Hamiltonian  $H_1(\varphi, \lambda) = \int_{\Omega} (-\varphi \nabla \lambda \cdot \nabla V) d^2 \mathbf{z}$  (where

for ease of notation we use the potential  $V(\mathbf{z}) = \left. \frac{\delta E(\mathbf{z})}{\delta \varphi} \right|_{\varphi}$ )

energy  $E(\varphi) = \int_{\Omega} \left[ U(\varphi(\mathbf{z})) + \frac{\epsilon}{2} \|\nabla\varphi(\mathbf{z})\|^2 \right] d^2\mathbf{z}$ , the transport paths corresponding to the optimal pattern evolution under the total Hamiltonian  $H = H_0 + H_1$  (see [Note S3.2](#) for details) are given by

$$\frac{d}{dt} \mathbf{x}(t) = -\nabla U(\mathbf{x}(t)) - \frac{1}{\gamma_u} e^{\int_0^t \nabla \nabla U(\mathbf{x}(\tau)) d\tau} \nabla \Lambda_0(\mathbf{x}_0), \mathbf{x}^{\text{nom}}(0) = \mathbf{x}_0^{\text{nom}} \quad (\text{Equation 22})$$

whereas before  $\Lambda_0$  is specified by the terminal constraints  $\phi_0$  and  $\phi^*$  on the pattern evolution. Comparing [Equations 21](#) and [22](#), we see that the straight transport paths (geodesics) associated with steering an initial pattern in the absence of physics via control are reshaped in the presence of physics, embodied in a potential, with the curvature of the transport paths determined by the Hessian of the potential  $V$ .<sup>52</sup> To see this, we note that differentiating [Equation 21](#) leads to  $\frac{d^2}{dt^2} \mathbf{x}^{\text{nom}}(t) = 0$ , while differentiating [Equation 22](#) yields  $\frac{d^2}{dt^2} \mathbf{x}(t) = \nabla \nabla U(\mathbf{x}(t)) \nabla U(\mathbf{x}(t)) = -\nabla \left( -\frac{1}{2} \|\nabla U\|^2 \right)$ . In other words, the emergent optimal path of pattern evolution in the presence of a force field is controlled by an effective potential  $V_{\text{eff}}(\mathbf{z}) = -\frac{1}{2} \|\nabla U(\mathbf{z})\|^2$ , identical to that seen in the optimal control of interactive active particles on complex landscapes (see [Equation 14](#)) but now is shown to be valid for fields as well. In [Figure 5](#) (bottom-right panel), we show the effect of passive physics, i.e., with  $\mathbf{v} \neq 0$ , the geometry of transport paths is curved, with  $\kappa(t) \neq 0$ .

More generally, Model B dynamics with non-linear forms of the mobility are known to arise in a range of systems such as dewetting transitions in droplets and motility-induced phase separation, and our approach is easily generalizable to those systems as well. As an example (see [Note S5](#) for details), the dewetting of a fluid on a substrate corresponds to Model B dynamics with the mobility given by  $m(\varphi) = \varphi^3$ , and the dewetting velocity field is given by  $\mathbf{v} = -\nabla \left( \frac{\delta E}{\delta \varphi} \right)$ , where  $E(\varphi) = \int_{\Omega} \left[ U(\varphi(\mathbf{z})) + \frac{\epsilon}{2} \|\nabla\varphi(\mathbf{z})\|^2 \right] d^2\mathbf{z}$ . In this case, the transport paths corresponding to the nominal Hamiltonian will themselves have non-zero curvature owing to the non-linear mobility, and a geometric interpretation of the control trajectory requires us to go beyond the simple considerations here, although a numerical approach is implementable (see results in [Note S5](#), [Figure S3](#), and [Video S3](#)).

## Numerical experiments

### Control of particles

To demonstrate the application of our algorithm, we present a series of numerical experiments illustrating optimal control of particle systems under different regimes. All simulations were implemented using JAX<sup>29</sup> for automatic differentiation and Diffrax<sup>49</sup> for numerical integration of stochastic and ordinary differential equations (SDEs and ODEs). The APIC algorithm was efficiently parallelized using JAX's vectorization tools (`vmap`).

[Figure 4A](#) shows a control task involving a single particle navigating a static Gaussian mixture potential landscape. Regions of high potential are shown in red and low potential in yellow. The

particle starts at the point (0.1, -0.3) and must reach the target at the origin (0,0), with the two separated by a potential ridge. Four trajectories are shown for different time horizons  $T = 0.01, 0.05, 0.1, \text{ and } 0.12$ . For small  $T$ , the particle follows a nearly straight path, but as  $T$  increases, the trajectories curve to avoid high potential regions. This demonstrates that with longer available time, the control strategy allows the particle to exploit the landscape geometry to reduce energy costs. The upper-right inset shows the magnitude of the control  $|\mathbf{u}(t)|$  on a log-linear scale, plotted against scaled time  $t^* = t/T$ . As expected, longer time horizons lead to smaller control amplitudes. The lower-right inset shows the total work  $W = \int_0^T \|\mathbf{u}\|^2 dt$  as a function of  $T$ , confirming the predicted inverse scaling  $W \sim 1/T$ , consistent with dimensional analysis and linear response theory.<sup>53,54</sup> For animations, see [Video S1](#).

In [Figure 4B](#), we examine the potential energy of the system as a function of scaled time for several different  $T$ . The uncontrolled system (green curve) relaxes with a characteristic time of approximately 0.08, visible as an exponential decay. In contrast, the controlled dynamics for  $T = 0.1$  exhibit a monotonic increase in energy, indicating a “spread-only” phase. For  $T = 0.5$  and  $T = 1$ , the energy initially decreases (a “gather” phase) before increasing again (a “spread” phase), with the  $T = 1$  case showing a more complete gather to near-zero energy. These behaviors reflect the time-dependent structure of the optimal control: longer horizons afford a richer two-phase strategy that balances energetic efficiency with task completion. For animations, see [Video S2](#).

[Figures 4C](#) and [4D](#) show the results of controlling a small network of five interacting particles connected by linear springs, navigating the same static Gaussian mixture potential. The inter-particle potential takes the form  $V(\mathbf{x}) = \frac{1}{2} \sum_{i=1}^N \sum_{j \in NN(i)} K (\|\mathbf{x}_i - \mathbf{x}_j\| - \ell)^2$ , with  $K$  the spring constant,  $\ell = 0.2$  the rest length, and  $NN(i)$  the set of nearest neighbors determined via a distance threshold of 1.5 units. [Figure 4C](#) shows the result for low diffusivity and stiffness ( $D = 0.0001, K = 0.0001$ ), while [Figure 4D](#) shows the case of higher noise and stiffness ( $D = 0.01, K = 0.1$ ). In both cases, the system tends to avoid high-potential regions, as predicted by the theory. However, the structural evolution differs: in the low- $D$ , low- $K$  regime, the particle cluster remains coherent, maintaining shape while traversing the ridge. In the high- $D$ , high- $K$  regime, the particle network spreads significantly and exhibits more erratic control behavior. Insets in each panel show the center-of-mass distance to the target and the magnitude of control across particles, confirming the quantitative differences in strategy. These results suggest that the APIC algorithm naturally adapts to both low-noise coherent steering and high-noise stochastic actuation in soft-interacting systems. For animation, see [Video S3](#).

### Control of spatiotemporal fields

We apply our control framework across several canonical pattern-forming systems arising in physical chemistry, soft matter, materials science, and biology. In all cases considered, the uncontrolled (passive) dynamics can be expressed as a gradient flow on a suitable free-energy functional. For instance, mass-conserving dynamics (as in the Cahn-Hilliard equation) and

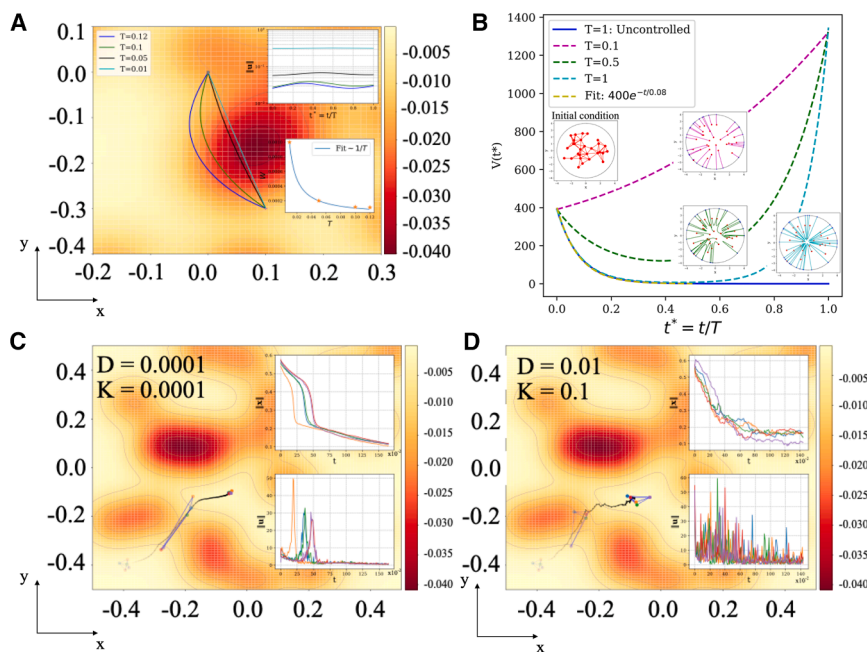


**Figure 4. Optimal control of athermal and fluctuating interacting particles**

(A) Regions of high potential are red in color, whereas yellow highlights regions of minimal potential (for details, see main text). In this control task, the particles underwent athermal dynamics under the influence of the frozen landscape. The control task was to move from the initial location (0.1, -0.3) to final point (0, 0). The task was chosen as the initial and final locations are separated from a potential barrier. From left to right, the curves correspond to particle trajectories corresponding to different time horizons:  $T = 0.12, T = 0.1, T = 0.05$  and  $T = 0.01$ . The plot shows as the time horizon is increased, the particle undergoes curved trajectories to escape regions of high potential. Inset on the upper right shows control magnitude,  $|u|$ , as a function of scaled time,  $t^* = \frac{t}{T}$ , for the numerical experiment in the main figure on a log-linear plot. The time has been scaled so that experiments corresponding to different time horizons can be plotted on the same graph. From bottom to top, the curves correspond to controls for  $T = 0.12, 0.1, 0.05$ , and  $0.01$ . The control for  $T = 0.12$  is approximately two orders of magnitude smaller than for  $T = 0.01$ . Inset on the lower right shows the magnitude to total work as a function of time

horizon,  $T$ . The orange stars correspond to the numerical experiment, whereas the blue line corresponds to the fit,  $W \sim \frac{1}{T}$ , estimated from theory. See [Video S1](#) for the simulation.

(B) Plot of potential energy,  $V$ , as a function of scaled time,  $t^* = \frac{t}{T}$ . As before, time has been scaled to plot the curves corresponding to different  $T$  on the same graph. The uncontrolled system (green line) undergoes relaxation with a characteristic timescale of approximately 0.08 units (shown as an exponential fit in cyan). Potential energy for  $T = 0.1$  shows a monotonic increase throughout the experiment corresponding to just the “spread” phase. Potential energy for both  $T = 0.5$  (blue) and  $T = 1$  (red) undergoes an initial decrease, corresponding to the “gather” phase, then a monotonic increase corresponding to “spread” phase. The gather spread in the  $T = 1$  case is more pronounced than in the  $T = 0.5$  case, as the potential energy approximately decreases to zero for the former. See [Video S2](#) for the simulation.

(C) Plot shows the trajectory of five interacting particles moving in a Gaussian mixture landscape for  $D = 0.0001$  and  $K = 0.0001$ . The top-right inset shows the distance of the particles from the origin, and the bottom-right inset shows the magnitude of the control for all the particles.

(D) Same as in (C) but for  $D = 0.01$  and  $K = 0.1$ . In both cases, the system of interacting particles move along ridges of the potential landscape, in accordance with [Equation 14](#). See [Video S3](#) for the simulation.

non-conserving dynamics (as in the Allen-Cahn equation) are both captured by the generalized evolution equation:

$$\frac{\partial \phi}{\partial t} = D_{\xi} \Delta \phi + \beta_1 \nabla \cdot \left( m(\phi) \nabla \frac{\delta E}{\delta \phi} \Big|_{\varphi = \phi} \right) - \beta_2 \frac{\delta E}{\delta \phi} \Big|_{\varphi = \phi}, \quad (\text{Equation 23})$$

where  $m(\varphi)$  is a mobility function,  $D_{\xi}$  is a diffusive term from microscopic noise, and  $\delta E / \delta \varphi$  is the variational derivative of the free-energy functional. This formalism provides a physically grounded continuum model for pattern formation in soft matter, active media, and biological tissues.

Control is introduced by augmenting these dynamics with active fluxes and source terms, as specified in [Equation 5](#).

(1) Phase separation: we consider two classic cases of phase separation dynamics governed by double-well free-energy densities.

- In the non-conserved case, with  $\beta_1 = 0, \beta_2 > 0$ , and  $D_{\xi} = 0$ , the order parameter evolves via local relaxation, yielding the Allen-Cahn equation (Model A).<sup>5,55</sup>
- In the conserved case, with  $\beta_1 > 0, \beta_2 = 0$ , and constant mobility, the system follows the Cahn-Hilliard equation

(Model B),<sup>5,55</sup> conserving the spatial integral of the order parameter.

(2) Morphogenesis: we group together two systems under the broad theme of biological pattern formation and differentiation.

- Reaction-diffusion systems consist of coupled fields evolving under diffusion and non-linear local reactions, leading to instabilities such as those predicted by Turing.<sup>6</sup> These provide classical models for spatial patterning in chemical and biological systems.
- Cell-fate dynamics are modeled by assigning internal states (fates) to mobile agents, whose evolution couples local signaling to spatial position. This leads to emergent differentiation patterns and spatial organization in tissues, capturing key aspects of developmental morphogenesis.

These systems, while diverse in microscopic detail, share a unifying structure as gradient flows on energy landscapes. Our framework allows them to be treated within the same optimal control formulation, making it broadly applicable to physical and biological pattern formation. Extensions to more complex

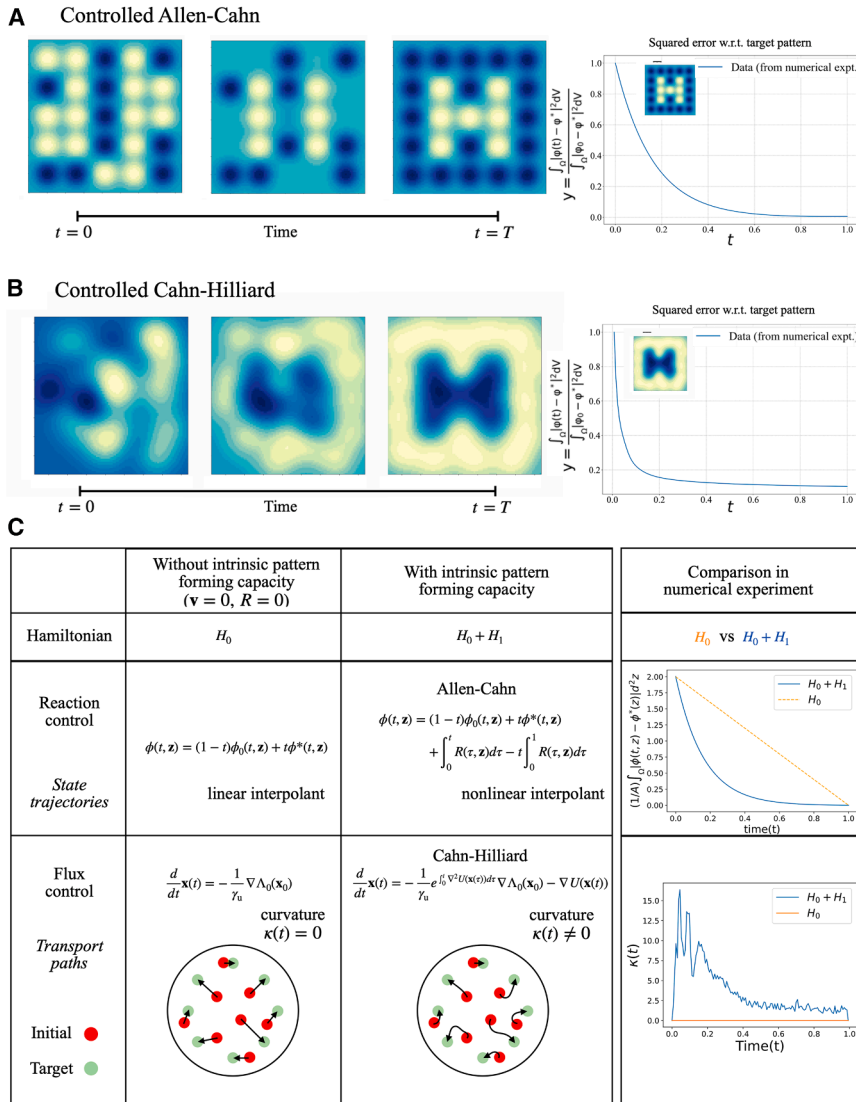


**Figure 5. Targeted phase separation and geometry of transport paths for pattern control**

(A) Controlling the phase separation of two species (blue and white colors) in a square lattice checkerboard pattern) governed by the Allen-Cahn Equation. The Eulerian pattern error and the target pattern “H” (inset) is shown on the rightmost panel. See [Video S4](#) for the simulation. (B) Controlling the phase separation of two species (blue and white colors from a randomly distributed initial condition) governed by the Cahn-Hilliard equation. The Eulerian pattern error and the target pattern “H” (inset) is shown on the rightmost panel. See [Video S5](#) for the simulation. (C) Pattern-forming capacity implied by the physics changes the geometry of the transport paths underlying optimal pattern evolution, as seen in [Equations 20, 21, and 22](#). The row corresponding to reaction control shows the optimal interpolant in pattern space for the case of a non-conserved order parameter, corresponding to the nominal Hamiltonian  $H_0(\varphi, \lambda)$  (see text above [Equation 20](#)) and with intrinsic pattern-forming capacity encoded in the Hamiltonian  $H_1(\varphi, \lambda)$  (see text above [Equation 20](#)). The row corresponding to flux control shows the ordinary differential equation underlying the transport paths for the case of a conserved order parameter, corresponding to the nominal Hamiltonian  $H_0(\varphi, \lambda)$  (see text above [Equation 21](#)). The top-left panel corresponds to the zero passive reaction field which leads to a linear interpolation of the patterns. The top-middle panel corresponds to a non-linear interpolation of the pattern when the reaction field is present (control of Allen-Cahn). The bottom-middle panel corresponds to the addition of a Hamiltonian for the intrinsic pattern-forming capacity  $H_1(\varphi, \lambda)$  (control of Cahn-Hilliard, see text above [Equation 22](#)). The rightmost column corresponds to the comparison in numerical experiments. In the rightmost column, we plot the mean target error between the optimal interpolant and target pattern as a function of time for the reaction control case (top-right panel)

corresponding to the Allen-Cahn dynamics, and the curvature of the transport paths as a function of time for flux control corresponding to the Cahn-Hilliard dynamics.

systems, including active matter with self-driven components,<sup>56</sup> follow naturally within this unified description.

### Controlling phase separation

We start by considering the case of controlling phase separation for the case of the dynamics associated with either a non-conserved order parameter (Model A: Allen-Cahn), or a conserved order parameter (Model B: Cahn-Hilliard). For Model A dynamics (Allen-Cahn), the (uncontrolled) phase field  $\phi(t, \mathbf{z})$  satisfies the equation  $\phi_t = \phi - \phi^3 + \Delta\phi$  (and corresponds to the energy functional  $E(\varphi) = \int_{\Omega} \left[ (1 - \varphi^2)^2 + \frac{\epsilon}{2} \|\nabla\varphi(\mathbf{z})\|^2 \right] d^2\mathbf{z}$ , with  $\mathbf{v} = 0$  and  $R = -\frac{\delta E}{\delta\varphi}$  in [Equation 1](#). For Model B dynamics (Cahn-Hilliard), the (uncontrolled) phase field  $\phi(t, \mathbf{z})$  satisfies the equation  $\phi_t = \Delta(-\phi + \phi^3 - \Delta\phi)$  (corresponding to the velocity field  $\mathbf{v} = -\frac{\delta E}{\delta\varphi}$  and the reaction field  $R = 0$  in [Equation 3](#)).

In either case, we assume that the initial condition is a random distribution given by  $\phi_0$  (see leftmost panels in [Figures 5A and 5B](#)) and the final target distribution,  $\phi^*$ , is in the form of the letter “H” (see inset in the right panels of [Figures 5A and 5B](#)). We see that as the (flux/reaction) control fields pushes the pattern toward the target, the error decreases approximately exponentially (power law) in time for Allen-Cahn (Cahn-Hilliard) (see the inset [Figure S1](#) and [Videos S4 and S5](#) for simulations of the controlled Allen-Cahn and Cahn-Hilliard systems, respectively). A variant of Model B dynamics but with a nonlinear mobility follows from a hydrodynamic model for droplet splitting and merger in the lubrication limit and falls within our framework (see [Note S6, Figure S2, and Videos S6 and S7](#) for simulations).

### Controlling morphogenesis

We now turn to two examples inspired by reaction-diffusion systems in chemistry and engineering<sup>57</sup> and morphogenetic

systems in developmental biology<sup>58–60</sup> and engineered mimics thereof. Indeed, recent experimental work shows that it is possible to control patterns in reaction-diffusion experiments using empirical methods<sup>57</sup> and similarly in developmental systems,<sup>61</sup> raising the question of how to do so in a principled manner. This necessitates increasing the complexity by steering patterns using both conserved (flux-like) and non-conserved (reaction-like) controls. We consider two examples: (1) a system of morphogens encoded via color, e.g., R, G, B, governed by a reaction-diffusion where the reaction term has quadratic non-linearity; and (2) a phenomenological model for determining cell-fate control that links internal cell states with that of their external positions, i.e., their neighborhood.

(1) Control of reaction-diffusion systems. Consider a pattern composed of three morphogen fields represented as  $\phi(t, \mathbf{z}) = (\phi_1(t, \mathbf{z}), \phi_2(t, \mathbf{z}), \phi_3(t, \mathbf{z}))$ , where  $\phi_i(t, \mathbf{z})$  is the concentration of the  $i$ th morphogen at a location  $\mathbf{z} \in \Omega \subset \mathbb{R}^2$  at time  $t \in [0, T]$ . We first define an energy functional with a cubic coupling so that the kinetic equations have quadratic non-linearities, given by

$$E(\varphi) = \int_{\Omega} \left[ \frac{1}{2} \sum_i D_i \|\nabla \varphi_i\|^2 - \frac{1}{3} \sum_{i,j,k=1}^3 M_{ijk} \varphi_i \varphi_j \varphi_k \right] d^2 \mathbf{z},$$

where  $i \in (1, 2, 3)$ ,  $D_i$  is the diffusion constant corresponding to the  $i$ th morphogen, and the term  $\sum_{i,j,k=1}^3 M_{ijk} \phi_i \phi_j \phi_k$  is a cubic polynomial with  $M_{ijk}$  a symmetric third-order tensor. Note that  $\varphi$  denotes an arbitrary field, whereas  $\phi$  denotes a trajectory. The passive forward reaction-diffusion dynamics for the  $i$ th morphogen is given by

$$\frac{\partial \phi_i}{\partial t} = - \left( \frac{\delta E}{\delta \phi} \Big|_{\phi} \right)_i = D_i \Delta \phi_i + \sum_{j,k=1}^3 M_{ijk} \phi_j \phi_k.$$

The optimal control problem for the reaction-diffusion system then reads as

$$\begin{aligned} \min_{\mathbf{u}, \mathbf{S}} & \frac{\gamma_u}{2} \int_0^T \int_{\Omega} \left( \sum_{i=1}^3 \phi_i(t, \mathbf{z}) \right) \|\mathbf{u}(t, \mathbf{z})\|^2 d^2 \mathbf{z} dt \\ & + \frac{\gamma_v}{2} \sum_{i=1}^3 \int_0^T \int_{\Omega} S_i^2(t, \mathbf{z}) d^2 \mathbf{z} dt + \Psi(\phi^{(T)}) \end{aligned}$$

$$\text{s.t. } \frac{\partial \phi_i}{\partial t} + \nabla \cdot (\phi_i \mathbf{u}) = D_i \Delta \phi_i + \sum_{j,k=1}^3 M_{ijk} \phi_j \phi_k + S_i, i = 1, 2, 3.$$

(Equation 24)

We use the smoothed particle hydrodynamics-based approach to convert the problem to a Lagrangian framework (see Note S4 for details) and then deploy our adjoint path-integral approach to solve the resulting large system. In our numerical experiments (see Note S6 for details on discretization), for simplicity, we assume  $D_1 = D_2 = D_3$  and further that  $M_{ijk}$  is a third-order tensor whose elements are sampled from a normal distribution with mean zero and unit variance. Figure 6A shows the results of an experiment where we steer an initially random pattern of  $\phi_i$ s encoded via color, e.g., R, G, B, to the pattern

“H,” where the left (right) vertical line is red (blue) and the center horizontal line is green (see Video S8).

(2) Control of cell-fate dynamics. We finally turn to a question inspired by biological morphogenesis wherein the fates and positions of active cells in a multicellular tissue are organized spatiotemporally in a reproducible way.<sup>62,63</sup> Since cell fates are intimately related to gene-expression patterns within a cell, which are themselves partly steered by their extracellular environment, a natural framework requires us to couple the external dynamics of motile cells and their internal states. Indeed, this framework might be relevant to an even broader class of active systems consisting of particles that can have multiple internal states while also capable of moving autonomously, with the states and movements being coupled to each other, e.g., in active matter systems,<sup>64</sup> or traveling waves of differentiation and movement in embryo development.<sup>58</sup> In a minimal setting, we model a two-dimensional epithelial layer undergoing the process of differentiation associated with the control of cell fate and position starting from a pluripotent state. Consider cells with spatial density function  $\rho(t, \mathbf{z})$  and a spatial gene-expression profile  $\phi(t, \mathbf{z})$  at time  $t$  and  $\mathbf{z} \in \Omega$ . For simplicity we assume that a particular gene in each cell can take on three values  $\{-1, 0, 1\}$ , where the value 0 corresponds to the undifferentiated pluripotent state and the values  $-1, 1$  correspond to two distinct differentiated states. Spatial coarse graining toward a long-wavelength continuum theory allows us to relax this discrete set to a continuum so that the gene-expression state  $-1 \leq \phi(t, \mathbf{z}) \leq 1$ . The optimal control problem of creating a non-equilibrium patterned tissue with a specific spatially differentiated phenotype can then be cast as

$$\begin{aligned} \min_{\mathbf{u}, \mathbf{S}} & \frac{\gamma_u}{2} \int_0^T \int_{\Omega} \rho(t, \mathbf{z}) \|\mathbf{u}(t, \mathbf{z})\|^2 d^2 \mathbf{z} dt \\ & + \frac{\gamma_v}{2} \int_0^T \int_{\Omega} \rho(t, \mathbf{z}) S^2(t, \mathbf{z}) d^2 \mathbf{z} dt + \Psi(\rho^{(T)}, \phi^{(T)}) \\ \text{s.t. } & \begin{cases} \frac{\partial \rho}{\partial t} + \nabla \cdot \left[ \rho \left( - \nabla \left( \frac{\delta E}{\delta \rho} \right) + \mathbf{u} \right) \right] = 0 \\ \frac{\partial \phi}{\partial t} + \left[ - \nabla \left( \frac{\delta E}{\delta \phi} \right) + \mathbf{u} \right] \cdot \nabla \phi = - \frac{\delta E}{\delta \phi} + S \end{cases} \end{aligned}$$

(Equation 25)

where the energy functional  $E$  is given by

$$E(\mathbf{q}, \varphi) = \int_{\Omega} (f(\mathbf{q}) + g(\mathbf{q}) \|\nabla \varphi\|^2) d^2 \mathbf{z}.$$

We note that the intercellular interaction consists of a long-range attraction ( $f(\rho)$ ) and short-range repulsion ( $g(\rho)$ ) between different cell types (see Note S7 for both the discretized version of the problem and the exact form of  $E(\mathbf{q}, \varphi)$ ). The first part of Equation 25 describes the dynamics of the controlled cell population as it progresses due to a combination of internal dynamics and external control (here we assume that total cell number is conserved, even though cell type is not), while the second part describes the dynamics of cell fate, which is advected at a velocity determined by active cell movement while simultaneously

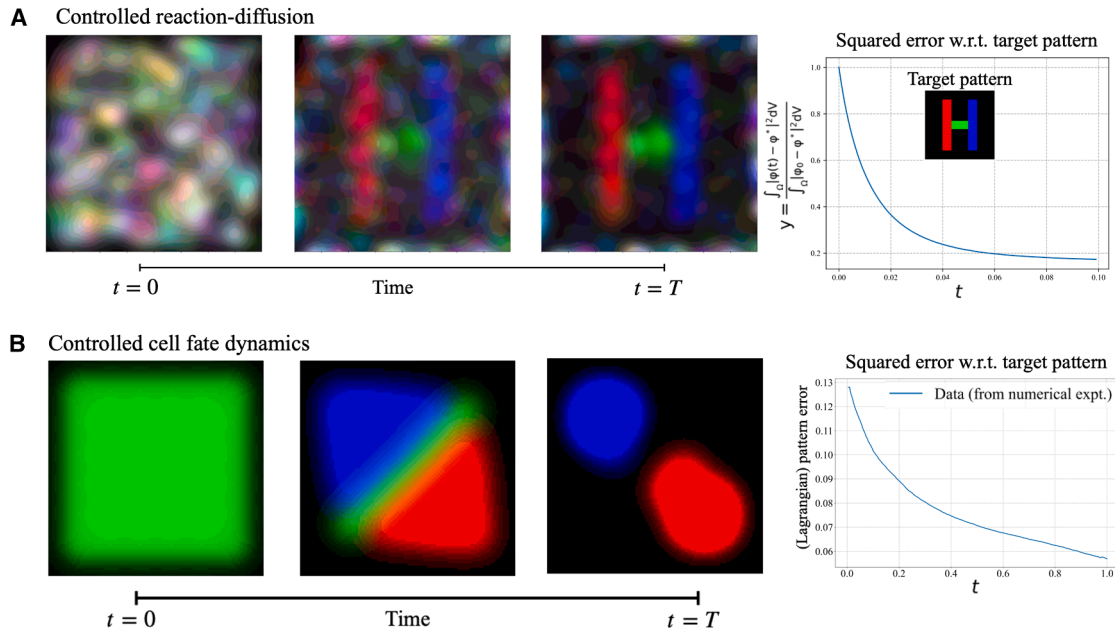


**Figure 6. Targeted morphogenesis**

(A) Control of a reaction-diffusion system. Controlling a reaction-diffusion system comprising three species, from a randomly generated reaction matrix and initial conditions (see [Note S7](#) for details). The uncontrolled reaction-diffusion system is given by [Equation 24](#). The rightmost panel shows that the evolution of the Lagrangian squared error (normalized with reference to initial error) relative to target pattern decays approximately exponentially (inset shows the H-shaped target pattern with the vertical and horizontal bars to be formed by the three individual species, respectively). See [Video S8](#) for the simulation.

(B) Control of cell-fate dynamics. The three panels are the representative intermediate patterns corresponding to the controlled cell fate decision making model given by [Equation 25](#). The figure on the left is the initial pluripotent state, the figure in the middle is the snapshot of the dynamical system at time  $T/2$ , and the rightmost figure is the snapshot of the dynamical system at time  $T$ . The rightmost panel shows that the evolution of the Lagrangian pattern error (normalized with reference to initial error) relative to target pattern decays approximately exponentially. See [Video S9](#) for the simulation.

being changed via reactive terms associated with the effect of the local cell population as well as external control. The terminal penalty is given by

$$\Psi(\mathbf{Q}, \varphi) = \frac{\delta_c}{4} \int_{\Omega} \prod_{k=1}^2 (\varphi - C_k)^2 \mathcal{Q} d^2 \mathbf{z} + \frac{\delta_\mu}{2} \int_{\Omega} \sum_{k=1}^2 e^{-\frac{(\varphi - C_k)^2}{2\sigma^2}} \|\mathbf{z} - \mu_k^*\|^2 \mathcal{Q} d^2 \mathbf{z},$$

where  $C_k = \{-1, 1\}$  characterizes the final differentiated states at spatial location  $\mu_k^*$  (where  $k = 1, 2$  corresponds to the differentiated states  $-1$  and  $1$ ), and  $\sigma$  sets the spatial range of specificity of the morphogen to the gene-expression state. The first term in the terminal cost corresponds to differentiation and penalizes undifferentiated (internal) terminal states, while the second term corresponds to segregation and penalizes deviation from (external) target locations for the population.

Using our SPH approach, we convert the above Eulerian description to a Lagrangian one and deploy our algorithm for stochastic optimal control (see [Note S4](#) for the SPH approach and [Note S7](#) for the discrete problem formulation). [Figure 6B](#) shows the sequential time snapshots of the controlled dynamical system where the cells undergo differentiation from a homogeneous pluripotent state (green) to a differentiated spatially segregated state (see [Video S5](#)) as the area of the differentiated states

(i.e., red and blue) initially increases and then reaches a steady state in time as cells simultaneously differentiate and migrate to specific target sites (see [Video S9](#)).

## DISCUSSION

Our study provides a framework to formulate and solve inverse design problems associated with pattern control in non-equilibrium physical, chemical, and biological systems. We show how minimizing control costs and terminal target-driven goals converts predictive theories for long-wavelength pattern formation—themselves grounded in conservation laws and symmetry/broken symmetry—into problems in stochastic optimal control theory for spatiotemporal fields. By accounting for physical priors embodied in terms of pattern formation dynamics, it also generalizes the classical optimal transport perspective,<sup>8</sup> which does not account for these dynamical constraints imposed by physics.

A Eulerian-Lagrangian mapping allows us to convert the field theory into a scale-dependent approximate many-body control problem that can be solved numerically using continuous time backpropagation methods originally devised for finite-dimensional systems.<sup>65,66</sup> Our numerical experiments demonstrate the effectiveness of our physics-driven generative framework for a range of pattern-forming systems that include phase separation with and without a conserved order parameter and morphogenetic processes involving reaction-diffusion and

activity. Our framework thus suggests a mechanism for how we can drive pattern-forming capacity in a system that starts out having none by using optimal control to create a series of way points (rather than a single terminal cost) in a closed-loop feedback system to drive forward physics step by step.

Finally, we close with a view of what might be next. First, traditional theory-rich approaches to pattern formation have relied on physical intuition and domain expertise to create coarse-grained phenomenological models,<sup>67</sup> combined with analytical and numerical techniques. Recent data-rich advances in generative models have opened up new data-driven avenues for studying and manipulating patterns.<sup>68</sup> Our approach naturally suggests an inference engine for generating and controlling patterns using physics-based priors (when available) along with experiments (to guide parameter choices and unknown physics) using optimal control and forward-backward algorithms that can be efficiently deployed across scales and systems.

Second, connecting our approach to experiments is another avenue for further exploration. Areas where the gap is bridgeable include (1) chemical microreactor control for DNA-based engineering (Simmel and Schulman<sup>69</sup> and references therein), (2) control of active nematics for cargo transport (Nishiyama et al.<sup>70</sup> and references therein), (3) epithelial morphogenesis (Huycke et al.<sup>71</sup> and references therein), and (4) deployment trajectories for origami/kirigami patterns (Hawkes et al.<sup>72</sup> and references therein). In each case, the underlying particle or field dynamics is known and capable of being steered via an external control, fitting perfectly into our general framework. The next steps would involve implementing our algorithmic protocols to achieve these goals in practical settings and scaling up our interpretable algorithms for the fast multiscale control of particles and fields.

## METHODS

The main text provides details about the APIC algorithm, and further details regarding the methods can be found in [supplemental information](#).

## RESOURCE AVAILABILITY

### Lead contact

Further information and requests regarding any resource should be directed to and will be fulfilled by the lead contact, L. Mahadevan ([lmahadev@g.harvard.edu](mailto:lmahadev@g.harvard.edu)).

### Materials availability

This study did not generate new materials.

### Data and code availability

The code for the numerical experiments can be found herein.

## ACKNOWLEDGMENTS

We acknowledge NSF grants BioMatter DMR 1922321, MRSEC DMR 2011754, and EFRI 1830901; the Simons Foundation; and the Henri Seydoux Fund, the Dana-Farber Cancer Institute (Prof. C.Z. Zhang), and the Wellcome Trust for partial financial support.

## AUTHOR CONTRIBUTIONS

V.K., S.S., and L.M. conceived the study; V.K., S.S., and L.M. created the APIC algorithm; V.K. and S.S. designed, coded, and simulated the APIC algorithm and generated all figures; and all authors discussed and interpreted the results and wrote the manuscript.

## DECLARATION OF INTERESTS

The authors declare no competing interests.

## SUPPLEMENTAL INFORMATION

Supplemental information can be found online at <https://doi.org/10.1016/j.newton.2025.100365>.

Received: November 13, 2024

Revised: July 15, 2025

Accepted: December 8, 2025

## REFERENCES

1. Shaebani, M.R., Wysocki, A., Winkler, R.G., Gompper, G., and Rieger, H. (2020). Computational models for active matter. *Nat. Rev. Phys.* 2, 181–199.
2. Landau, L. (1937). On the theory of phase transitions. *Zh. eksp. teor. Fiz* 7, 926.
3. Cross, M., and Greenside, H. (2009). *Pattern Formation and Dynamics in Nonequilibrium Systems* (Cambridge University Press).
4. Desai, R., and Kapral, R. (2009). *Dynamics of Self-Organized and Self-Assembled Structures* (Cambridge University Press).
5. Balluffi, R., Allen, S., and Carter, C. (2005). *Kinetics of Materials* (John Wiley & Sons).
6. Murray, J.D. (2007). *Mathematical Biology: V. II17* (Springer Science & Business Media).
7. Jordan, R., Kinderlehrer, D., and Otto, F. (1998). The variational formulation of the fokker-planck equation. *SIAM J. Math. Anal.* 29, 1–17.
8. Benamou, J.D., and Brenier, Y. (2000). A computational fluid mechanics solution to the monge-kantorovich mass transfer problem. *Numer. Math.* 84, 375–393.
9. Sohl-Dickstein, J., Weiss, E., Maheswaranathan, N., and Ganguli, S. (2015). Deep unsupervised learning using nonequilibrium thermodynamics. In *International Conference on Machine Learning*, pp. 2256–2265.
10. Rout, L., Korotin, A., and Burnaev, E. (2021). Generative modeling with optimal transport maps. Preprint at arXiv. <https://doi.org/10.48550/arXiv.2110.02999>.
11. An, D., Guo, Y., Lei, N., Luo, Z., Yau, S.T., and Gu, X. (2019). AE-OT: A New Generative Model Based on Extended Semi-discrete Optimal Transport (ICLR).
12. Chizat, L., Peyré, G., Schmitzer, B., and Vialard, F.X. (2018). Unbalanced optimal transport: Dynamic and Kantorovich formulations. *J. Funct. Anal.* 274, 3090–3123.
13. Tabak, E.G., and Vanden-Eijnden, E. (2010). Density estimation by dual ascent of the log-likelihood. *Commun. Math. Sci.* 8, 217–233.
14. Tabak, E.G., and Turner, C.V. (2013). A family of nonparametric density estimation algorithms. *Commun. Pure Appl. Math.* 66, 145–164.
15. Rezende, D., and Mohamed, S. (2015). Variational inference with normalizing flows. In *International Conference on Machine Learning*, pp. 1530–1538.
16. Song, Y., Sohl-Dickstein, J., Kingma, D., Kumar, A., Ermon, S., and Poole, B. (2020). Score-based generative modeling through stochastic

- differential equations. Preprint at arXiv. <https://doi.org/10.48550/arXiv.2011.13456>.
17. Biroli, G., Bonnaire, T., Bortoli, V.D., and Mézard, M. (2024). Dynamical regimes of diffusion models. Preprint at arXiv. <https://doi.org/10.48550/arXiv.2011.13456>.
  18. Wiener, N. (2019). *Cybernetics: Or Control and Communication in the Animal and the Machine* (MIT press).
  19. Rosenblueth, A., Wiener, N., and Bigelow, J. (1943). Behavior, purpose and teleology. *Philos. Sci.* *10*, 18–24.
  20. Ellis, G.F.R., and Kopel, J. (2018). The dynamical emergence of biology from physics: branching causation via biomolecules. *Front. Physiol.* *9*, 1966.
  21. Rosenbrock, H.H. (2000). Doing quantum mechanics with control theory. *IEEE Trans. Automat. Contr.* *45*, 73–77.
  22. Stengel, R.F. (1986). *Stochastic Optimal Control: Theory and Application* (John Wiley & Sons, Inc).
  23. Kappen, H.J. (2005). Path integrals and symmetry breaking for optimal control theory. *J. Stat. Mech.* *2005*, P11011.
  24. Theodorou, E., and Todorov, E. (2012). Relative entropy and free energy dualities: Connections to path integral and KL control. In *IEEE Conference on Decision and Control*, pp. 1466–1473.
  25. Fleming, W.H., and Mitter, S.K. (1982). Optimal control and nonlinear filtering for nondegenerate diffusion processes. *Stochastics* *8*, 63–77.
  26. Bryson, A.E., and Ho, Y.C. (1975). *Applied Optimal Control: Optimization, Estimation and Control* (Routledge).
  27. Bryson, A.E., and Denham, W.F. (1962). A steepest-ascent method for solving optimum programming problems. *J. Appl. Mech.* *29*, 247–257.
  28. Rumelhart, D.E., Hinton, G.E., and Williams, R.J. (1986). Learning representations by back-propagating errors. *Nature* *323*, 533–536.
  29. Bradbury, J., Frostig, R., Hawkins, P., Johnson, M.J., Leary, C., Maclaurin, D., Necula, G., Paszke, A., VanderPlas, J., Wanderman-Milne, S., and Zhang, Q. (2018). JAX: Composable transformations of Python+NumPy programs. <http://github.com/google/jax>.
  30. Baydin, A.G., Pearlmutter, B.A., Radul, A.A., and Siskind, J.M. (2018). Automatic differentiation in machine learning: A survey. *J. Mach. Learn. Res.* *18*, 1–43.
  31. Theodorou, E., Buchli, J., and Schaal, S. (2010). A generalized path integral control approach to reinforcement learning. *J. Mach. Learn. Res.* *11*, 3137–3181.
  32. Williams, G., Aldrich, A., and Theodorou, E.A. (2017). Model predictive path integral control: From theory to parallel computation. *J. Guid. Control Dynam.* *40*, 344–357.
  33. Urbani, P. (2021). Disordered high-dimensional optimal control. *J. Phys. A: Math. Theor.* *54*, 324001.
  34. Engel, M.C., Smith, J.A., and Brenner, M.P. (2023). Optimal control of nonequilibrium systems through automatic differentiation. *Phys. Rev. X* *13*, 041032.
  35. Werschnik, J., and Gross, E.K.U. (2007). Quantum optimal control theory. *J. Phys. B: At. Mol. Opt. Phys.* *40*, R175–R211.
  36. Wolynes, P.G., Onuchic, J.N., and Thirumalai, D. (1995). Navigating the folding routes. *Science* *267*, 1619–1620.
  37. Zheng, W., Brooks, B.R., and Thirumalai, D. (2006). Low-frequency normal modes that describe allosteric transitions in biological nanomachines are robust to sequence variations. *Proc. Natl. Acad. Sci. USA* *103*, 7664–7669.
  38. Rocks, J.W., Pashine, N., Bischofberger, I., Goodrich, C.P., Liu, A.J., and Nagel, S.R. (2017). Designing allostery-inspired response in mechanical networks. *Proc. Natl. Acad. Sci. USA* *114*, 2520–2525.
  39. Iram, S., Dolson, E., Chiel, J., Pelesko, J., Krishnan, N., Güngör, Ö., Kuznets-Speck, B., Deffner, S., Ilker, E., Scott, J.G., and Hinczewski, M. (2021). Controlling the speed and trajectory of evolution with counterdiabatic driving. *Nat. Phys.* *17*, 135–142.
  40. Haggerty, D.A., Banks, M.J., Kamenar, E., Cao, A.B., Curtis, P.C., Mezić, I., and Hawkes, E.W. (2023). Control of soft robots with inertial dynamics. *Sci. Robot.* *8*, eadd6864.
  41. Zadpoor, A.A., Mirzaali, M.J., Valdevit, L., and Hopkins, J.B. (2023). Design, material, function, and fabrication of metamaterials. *APL Mater.* *11*, 020401.
  42. Stern, M., and Murugan, A. (2023). Learning without neurons in physical systems. *Annu. Rev. Condens. Matter Phys.* *14*, 417–441.
  43. Reid, D.R., Pashine, N., Wozniak, J.M., Jaeger, H.M., Liu, A.J., Nagel, S.R., and de Pablo, J.J. (2018). Auxetic metamaterials from disordered networks. *Proc. Natl. Acad. Sci. USA* *115*, E1384–E1390.
  44. Pashine, N., Hexner, D., Liu, A.J., and Nagel, S.R. (2019). Directed aging, memory, and nature’s greed. *Sci. Adv.* *5*, eaax4215.
  45. Rus, D., and Tolley, M.T. (2015). Design, fabrication and control of soft robots. *Nature* *521*, 467–475.
  46. Prasath, S.G., Mandal, S., Giardina, F., Kennedy, J., Murthy, V.N., and Mahadevan, L. (2022). Dynamics of cooperative excavation in ant and robot collectives. *eLife* *11*, e79638.
  47. Bahri, Y., Kadmon, J., Pennington, J., Schoenholz, S.S., Sohl-Dickstein, J., and Ganguli, S. (2020). Statistical mechanics of deep learning. *Annu. Rev. Condens. Matter Phys.* *11*, 501–528.
  48. Bellman, R. (1957). *Dynamic Programming* (Princeton University Press).
  49. Kidger, P. (2021). On Neural Differential Equations. Ph.D. thesis (University of Oxford).
  50. Cross, M.C., and Hohenberg, P.C. (1993). Pattern formation outside of equilibrium. *Rev. Mod. Phys.* *65*, 851–1112.
  51. Landau, L., and Lifshitz, E. (1960). *Mechanics1* (CUP Archive).
  52. Stern, M., Liu, A.J., and Balasubramanian, V. (2024). Physical effects of learning. *Phys. Rev. E* *109*, 024311.
  53. Sivak, D.A., and Crooks, G.E. (2012). Thermodynamic metrics and optimal paths. *Phys. Rev. Lett.* *108*, 190602.
  54. Blaber, S., and Sivak, D.A. (2023). Optimal control in stochastic thermodynamics. *J. Phys. Commun.* *7*, 033001.
  55. Hohenberg, P.C., and Halperin, B.I. (1977). Theory of dynamic critical phenomena. *Rev. Mod. Phys.* *49*, 435–479.
  56. Tailleur, J., Gompper, G., Marchetti, C., Yeomans, J., and Salomon, C. (2022). *Active Matter and Nonequilibrium Statistical Physics: Lecture Notes of the Les Houches Summer School1712* (Oxford University Press).
  57. Scalise, D., and Schulman, R. (2019). Controlling matter at the molecular scale with dna circuits. *Annu. Rev. Biomed. Eng.* *21*, 469–493.
  58. Di Talia, S., and Vergassola, M. (2022). Waves in embryonic development. *Annu. Rev. Biophys.* *51*, 327–353.
  59. Kicheva, A., and Briscoe, J. (2023). Control of tissue development by morphogens. *Annu. Rev. Cell Dev. Biol.* *39*, 91–121.
  60. Pezzotta, A., and Briscoe, J. (2023). Optimal control of gene regulatory networks for morphogen-driven tissue patterning. *Cell Syst.* *14*, 940–952.e11.
  61. Rossant, J. (2018). Genetic control of early cell lineages in the mammalian embryo. *Annu. Rev. Genet.* *52*, 185–201.
  62. Shim, G., Devenport, D., and Cohen, D.J. (2021). Overriding native cell coordination enhances external programming of collective cell migration. *Proc. Natl. Acad. Sci. USA* *118*, e2101352118.
  63. Qiu, X., Zhang, Y., Martin-Rufino, J.D., Weng, C., Hosseinzadeh, S., Yang, D., Pogson, A.N., Hein, M.Y., Hoi Joseph Min, K., Wang, L., et al. (2022). Mapping transcriptomic vector fields of single cells. *Cell* *185*, 690–711.e45.
  64. Marchetti, M.C., Joanny, J.F., Ramaswamy, S., Liverpool, T.B., Prost, J., Rao, M., and Simha, R.A. (2013). Hydrodynamics of soft active matter. *Rev. Mod. Phys.* *85*, 1143–1189.

65. Chen, R., Rubanova, Y., Bettencourt, J., and Duvenaud, D. (2018). Neural ordinary differential equations. *Advances in Neural Information Processing Systems* *31*, 6572–6583.
66. Li, X., Wong, T.K., Chen, R., and Duvenaud, D. (2020). Scalable gradients for stochastic differential equations. In *International Conference on Artificial Intelligence and Statistics*, pp. 3870–3882.
67. Reeves, G.T., Muratov, C.B., Schüpbach, T., and Shvartsman, S.Y. (2006). Quantitative models of developmental pattern formation. *Dev. Cell* *11*, 289–300.
68. Yang, H. (2022). A mathematical framework for learning probability distributions. Preprint at arXiv. <https://doi.org/10.48550/arXiv.2212.11481>.
69. Simmel, F.C., and Schulman, R. (2017). Self-organizing materials built with dna. *MRS Bull.* *42*, 913–919.
70. Nishiyama, K., Berezney, J., Norton, M., Aggarwal, A., Ghosh, S., Zarei, Z., Hagan, M., Fraden, S., and Dogic, Z. (2025). Closed-loop control of active nematic flows. *Phys. Rev. X* *15*, 041053. <https://doi.org/10.1103/4hrx-6rdq>.
71. Huycke, T.R., Häkkinen, T.J., Miyazaki, H., Srivastava, V., Baruet, E., McGinnis, C.S., Kalantari, A., Cornwall-Scoones, J., Vaka, D., Zhu, Q., et al. (2024). Patterning and folding of intestinal villi by active mesenchymal dewetting. *Cell* *187*, 3072–3089.e20.
72. Hawkes, E., An, B., Benbernou, N.M., Tanaka, H., Kim, S., Demaine, E.D., Rus, D., and Wood, R.J. (2010). Programmable matter by folding. *Proc. Natl. Acad. Sci. USA* *107*, 12441–12445.